



Lannelli, A., Marcos, A., Bombardieri, R., & Cavallaro, R. (2019). Linear Fractional Transformation co-modeling of high-order aeroelastic systems for robust flutter analysis. *European Journal of Control*. <https://doi.org/10.1016/j.ejcon.2019.12.002>

Peer reviewed version

License (if available):  
CC BY-NC-ND

Link to published version (if available):  
[10.1016/j.ejcon.2019.12.002](https://doi.org/10.1016/j.ejcon.2019.12.002)

[Link to publication record in Explore Bristol Research](#)  
PDF-document

This is the author accepted manuscript (AAM). The final published version (version of record) is available online via Elsevier at <https://doi.org/10.1016/j.ejcon.2019.12.002>. Please refer to any applicable terms of use of the publisher.

## University of Bristol - Explore Bristol Research

### General rights

This document is made available in accordance with publisher policies. Please cite only the published version using the reference above. Full terms of use are available:  
<http://www.bristol.ac.uk/red/research-policy/pure/user-guides/ebr-terms/>

# Linear Fractional Transformation co-modeling of high-order aeroelastic systems for robust flutter analysis

Andrea Iannelli<sup>a,\*</sup>, Andrés Marcos<sup>b</sup>, Rocco Bombardieri<sup>c</sup>, Rauno Cavallaro<sup>c</sup>

<sup>a</sup>*Automatic Control Lab, Swiss Federal Institute of Technology, ETH, Zürich 8092, Switzerland*

<sup>b</sup>*Department of Aerospace Engineering, University of Bristol, Bristol, England BS8 1TR, United Kingdom*

<sup>c</sup>*Department of Bioengineering and Aerospace Engineering, Universidad Carlos III de Madrid, 28911 Leganés, Spain*

---

## Abstract

This article presents a new paradigm for robust flutter modeling and analysis of high-order uncertain and linear aeroelastic systems. The fundamental idea is to couple the state-of-art in robust worst-case analysis (Linear Fractional Transformation modeling and  $\mu$  analysis) with the state-of-practice in aeroelasticity (fluid-structure-interaction solvers). The issue with the latter is that, although capable of providing different levels of fidelity, they are less efficient in coping with the analysis of systems subject to uncertainties. In fact, while they have the advantage of capturing directly the physical uncertainty, the analyses can only be applied to a defined parameter combination, and due to their computational cost, it is usually only possible to consider a limited set of cases. To tackle this lack of robustness, in recent works the application of analytic worst-case methods has been proposed, but the intimately related problem of constructing accurate uncertain models has not been fully addressed. In this article, a co-modeling framework is presented that leverages the main features of both fluid-structure interaction solvers and robust control-based methods. The key idea is to combine these two typically distinct steps in a single one, enabling in this way to obtain an uncertainty description which is flexible and reconciles the physical sources of uncertainty with the uncertain parameters used in the LFT model. An exemplification of the developed framework on an unconventional aircraft configuration is provided. Results show its potential to provide valuable physical insights into the problem when analyzing complex systems.

*Keywords:* Linear Fractional Transformation; uncertain systems; robust modeling and analysis.

---

## 1. Introduction

Aeroelasticity studies the interaction of a flexible structure and a fluid. This is typically accomplished with fluid-structure interaction (FSI) solvers, describing the interplay between elastic deformation and aerodynamic loads by means of specialized dedicated tools. Among the aeroelastic phenomena, flutter is a self-excited dynamic instability which can provoke failure of the structure. For this reason, flutter has been widely studied and, nowadays, solution methodologies are quite established [1].

One of the main issues in the state-of-practice for flutter analysis originates from the sensitivity of this instability to modeling assumptions and to variations in the nominal values of the parameters. With the goal of providing the analyst with tools complementing the conventional approaches for nominal flutter analysis, in the last two decades researchers have looked at analytical modeling and analysis techniques from the robust control community, namely the Linear Fractional Transformation (LFT) model representation and the structured singular value (s.s.v.) or  $\mu$  analysis [2]. In essence, they represent a generalization of the linear stability (and performance) analysis for systems subject to uncertainties, which is performed in a deterministic and methodological manner. Robust flutter analysis aims to quantify the gap between the

---

\*Corresponding author

Email address: iannelli@control.ee.ethz.ch (Andrea Iannelli)

conditions at which the instability occurs when the model has no uncertainties and the worst-case scenario when uncertainties are considered. This represents a powerful tool when used as a complement to classical techniques in that it can highlight weak points of the model requiring refinement and conversely identify parameters that can be coarsely estimated as they do not have a strong influence on the results.

Foundational works are those from [3] and [4], which provided an end-to-end process, from robust modeling to analysis, and demonstrated the validity of the approach. More recently, in reference [5] the potential of the  $\mu$ -LFT framework in providing something more than a simple binomial-type prediction (that is, whether the system is robustly stable or not in the face of the defined uncertainties) was illustrated with application to aeroelastic instabilities characteristic of modern aircraft configurations. Complementing the latter work, reference [6] considered specific features of the LFT model development paths for aeroelastic systems and investigated the effect of different LFT modeling options. However, despite the research carried out on these approaches, physical based rationale to select the uncertainties and systematic methods to represent them as LFTs, which are effective regardless of the fidelity (or order) of the model, are still lacking in the community.

Driven by these objectives, this article formulates a novel co-modeling LFT-FSI framework, whose distinctive feature is to reconcile the advantages of robust control tools and aeroelastic solvers by combining these two classically separated steps in a single one. The main technical contribution (Section 4) consists of a *symbolic* LFT modeling algorithm, embedded in the FSI solver, which allows parametric uncertainty descriptions of generic complexity to be accurately captured and efficient  $\mu$  analysis to be subsequently applied. Specifically, the developed approach allows LFT models to be obtained with the uncertainties derived from physical parameters defined within the high-fidelity FSI solvers. It is noted that the connection between physical sources of uncertainty (well distinguishable in the original high-order system) and uncertain parameters captured in the LFT model is a paramount aspect, and yet this has not received full consideration. For example, in [3, 4] the uncertainties in the structural operators consisted of modal quantities (e.g. natural frequencies), whereas [7, 8] considered physical sources of uncertainties but the examples were restricted to a small number, and specific types, of parameters. In addition, prompted by the fact that the computation of lower bounds on  $\mu$  is the result of a non-convex optimization, an algorithm to check the optimality of the found worst-case perturbation matrix is also devised and its usage with the proposed iterative analysis algorithm formalised.

A second contribution (Section 3) is the discussion of an improved numerical LFT modeling strategy. This belongs to the class of commonly employed approaches for LFT modeling, but, compared to those found in the literature, new features are proposed here enable to enable considering a larger number of variables while keeping the ensuing robust analysis problem computationally tractable. This is achieved by exploiting the knowledge of the aeroelastic dynamics, and, most importantly, by introducing the idea of *modal-oriented* LFT modeling, which allows the definition of uncertainty only in a restricted number of structural modes.

While in this article application of  $\mu$  analysis is pursued, it is stressed that methods to construct accurate LFT models for high-order systems are of more general interest. Indeed, various techniques in robust control require such a characterization of the uncertainty, for example multi-plant synthesis [9, 10] and Integral Quadratic Constraints analysis [11, 12].

In order to exemplify the capability of the developed LFT-FSI framework, in Section 5 two case studies featuring a joined-wing aircraft of the Prandtlplane type [13] are considered. This aircraft layout has been chosen as demonstration platform because of its complex and only partially understood aeroelastic behaviour, which makes it a challenging test bed for the presented strategies [14]. Given the current interest in unconventional aircraft (due to their prospective advantages to tackle the challenges of contemporary aviation), the results showcased by the developed methods suggest that they can represent a useful tool to gain a more-in-depth understanding and allow a more efficient design process.

The article, which extends preliminary results published in [15], is structured as follows. Section 2 provides the essential background of the work. Section 3 discusses a numerical LFT methodology which addresses some of the shortcomings of the available methods. In Section 4 the LFT symbolic framework is detailed, and a comprehensive discussion on advantages and possible issues is presented. Section 5 demonstrates the application of the developed framework to the case studies, and Section 6 concludes the work.

## 2. Theory fundamentals & Tools

In this section a cursory overview of the robust control-based techniques used here, namely LFT modeling and  $\mu$  analysis, is given first. Then, a brief description of the fluid-structure interaction problem is provided with focus on the in-house solver employed in this work. This section also contains all the assumptions on the FSI model and the abbreviations used in the remainder of the paper.

### 2.1. Robust control theory: LFT modeling and $\mu$ analysis

Let  $\mathbf{M}$  be a matrix partitioned as  $\mathbf{M} = [\mathbf{M}_{11} \ \mathbf{M}_{12}; \ \mathbf{M}_{21} \ \mathbf{M}_{22}]$ . Let also indicate with  $\Delta$  a structured uncertainty set, i.e. a set defined as follows [2]:

$$\Delta^{x,R-y,C} = \text{diag}(\delta_{d_i}^R I_{k_{d_i}}, \delta_{d_j}^C I_{k_{d_j}}, \Delta_{D_z}^C) \quad (1)$$

where the uncertainties associated to repeated real scalars  $\delta_{d_i}^R$ , repeated complex scalars  $\delta_{d_j}^C$ , and full complex blocks  $\Delta_{D_z}^C$  are listed in diagonal format (and where  $I_{k_{d_i}}$  denotes the identity matrix of dimension  $k_{d_i}$  equal to the number of repetitions of the parameter). Total real and complex parameters gathered in  $\Delta$  are indicated respectively by  $(x, R)$  and  $(y, C)$ .

The upper LFT model of  $\mathbf{M}$  with respect to  $\Delta$  is:

$$\mathcal{F}_u(\mathbf{M}, \Delta) = \mathbf{M}_{22} + \mathbf{M}_{21} \Delta (\mathbf{I} - \mathbf{M}_{11} \Delta)^{-1} \mathbf{M}_{12} \quad (2)$$

The size of an LFT refers to the total dimension of the associated set  $\Delta$ , whereas the magnitude of a realization of  $\Delta$  will refer to its maximum singular value, i.e.  $\bar{\sigma}(\Delta)$  (with  $\Delta \in \Delta$ ).

If  $\mathbf{M}$  is taken as a proper transfer matrix, then  $\mathcal{F}_u$  is the closed-loop transfer matrix from input  $\mathbf{u}$  to output  $\mathbf{y}$  when the nominal plant (i.e. the system with no uncertainty)  $\mathbf{M}_{22}$  is subject to a perturbation matrix  $\Delta$ . A crucial feature, apparent in Eq. (2), is that the LFT is well posed if and only if the inverse of  $(\mathbf{I} - \mathbf{M}_{11} \Delta)$  exists.

In this work the focus is on parametric uncertainties, which can be used to describe parameters whose values are varying or not known within a satisfactory level of confidence. Considering a generic uncertain parameter  $d$ , with  $w_d$  indicating the uncertainty level with respect to a nominal value  $d_0$  and  $\delta_d \in [-1, 1]$  representing the normalized uncertainty value, a general uncertain representation is given by:

$$d = d_0(1 + w_d \delta_d) \quad (3)$$

This (scalar) expression is often referred to as *multiplicative* uncertainty [2]. At a matrix level, the operator  $\mathbf{D}$  which is affected by structured uncertainties  $\Delta_{\mathbf{D}}$  can be expressed as:

$$\mathbf{D} = \mathbf{D}_0(\mathbf{I} + \mathbf{W}_{\mathbf{D}} \Delta_{\mathbf{D}}) \quad (4)$$

where  $\mathbf{W}_{\mathbf{D}}$  is a scaling matrix gathering the uncertainty levels.

For analysis of uncertain systems, a well-established concept is the structured singular value (s.s.v.) [16], which is represented by  $\mu_{\Delta}(\mathbf{M})$  and defined as:

$$\mu_{\Delta}(\mathbf{M}) = \frac{1}{\min_{\Delta \in \Delta} \{ \kappa : \det(\mathbf{I} - \kappa \mathbf{M} \Delta) = 0; \ \bar{\sigma}(\Delta) \leq 1 \}} \quad (5)$$

where  $\Delta$  is the structured uncertainty set associated with  $\mathcal{F}_u(\mathbf{M}, \Delta)$ . For ease of calculation and interpretation, and without loss of generality, this set is norm-bounded by scaling of  $\mathbf{M}$ . Note that  $\mathbf{M}$  is a transfer matrix, thus  $\mu_{\Delta}(\mathbf{M})$  is a function of the frequency  $\omega$ .

The result of the robust stability (RS) test, as applied to a system represented by an  $\mathcal{F}_u(\mathbf{M}, \Delta)$ , can then be interpreted as follows: if  $\mu_{\Delta}(\mathbf{M}) < 1$  then there is no perturbation matrix inside the allowable set  $\Delta$  such that the determinant condition is satisfied. That is,  $\mathcal{F}_u(\mathbf{M}, \Delta)$  is well posed and thus the associated plant is robust stable within the range of uncertainties considered. On the contrary, if  $\mu_{\Delta}(\mathbf{M}) \geq 1$  a candidate (i.e.

belonging to the allowed set) perturbation matrix exists that violates the well-posedness, i.e. the uncertain system described by Eq. (2) is unstable.

It is known that  $\mu_{\Delta}(\mathbf{M})$  is in general an NP-hard problem [2], thus all  $\mu$  algorithms work by searching for upper (UB) and lower (LB) bounds. The upper bound  $\mu_{\text{UB}}$  provides the maximum size perturbation  $\bar{\sigma}(\Delta_{\text{UB}}) = 1/\mu_{\text{UB}}$  for which RS is guaranteed, whereas the lower bound  $\mu_{\text{LB}}$  defines a minimum size perturbation  $\bar{\sigma}(\Delta_{\text{LB}}) = 1/\mu_{\text{LB}}$  for which RS is guaranteed to be violated. It is emphasized here that the lower bound also provides a matrix  $\Delta_{\text{LB}} = \hat{\Delta}^{cr}$  satisfying the determinant condition. If the bounds are close in magnitude, then  $\Delta_{\text{LB}}$  is the worst-case matrix –i.e. the perturbation with the smallest magnitude leading to instability.

## 2.2. CSHELL: an advanced fluid-structure interaction solver

CSHELL is an FSI solver developed by the authors of references [17, 18]. Among the available implemented capabilities, in here only the modules and methods required for the proposed framework are described.

The equation governing the aeroelastic system in the frequency domain is written as:

$$[-\omega^2 \bar{\mathbf{M}}_{\mathbf{s}} + i\omega \bar{\mathbf{C}}_{\mathbf{s}} + \bar{\mathbf{K}}_{\mathbf{s}} - q_{\infty} \mathbf{Q}_{hh}(i\omega)] \boldsymbol{\eta} = 0 \quad (6)$$

where  $q_{\infty} = \frac{1}{2}\rho_{\infty}V_{\infty}^2$  is the dynamic pressure,  $\rho_{\infty}$  is the air density,  $V_{\infty}$  is the speed,  $\omega$  the frequency,  $\bar{\mathbf{M}}_{\mathbf{s}}$ ,  $\bar{\mathbf{C}}_{\mathbf{s}}$ ,  $\bar{\mathbf{K}}_{\mathbf{s}} \in \mathbb{R}^{n_s \times n_s}$  represent respectively the generalized structural mass, damping and stiffness matrices ( $n_s$  is the number of normal modes),  $\mathbf{Q}_{hh}$  is the generalized aerodynamic force (GAF) coefficient matrix, and  $\boldsymbol{\eta}$  the generalized coordinates vector. Flutter analysis studies the conditions at which the dynamic aeroelastic system (6), loses its stability. Specifically, the flutter speed  $V_f$  is the lowest value of  $V_{\infty}$  such that the system becomes unstable.

The generalized structural matrices are obtained with the modal decomposition approach from their finite element counterparts  $\mathbf{M}_{\mathbf{s}}$ ,  $\mathbf{C}_{\mathbf{s}}$ ,  $\mathbf{K}_{\mathbf{s}} \in \mathbb{R}^{N_s \times N_s}$ , with  $N_s$  indicating the number of structural independent degrees of freedom, as:

$$\begin{aligned} \bar{\mathbf{M}}_{\mathbf{s}} &= \boldsymbol{\Phi}^T \mathbf{M}_{\mathbf{s}} \boldsymbol{\Phi} \\ \bar{\mathbf{C}}_{\mathbf{s}} &= \boldsymbol{\Phi}^T \mathbf{C}_{\mathbf{s}} \boldsymbol{\Phi} \\ \bar{\mathbf{K}}_{\mathbf{s}} &= \boldsymbol{\Phi}^T \mathbf{K}_{\mathbf{s}} \boldsymbol{\Phi} \end{aligned} \quad (7)$$

where the modal matrix  $\boldsymbol{\Phi} \in \mathbb{R}^{N_s \times n_s}$  is obtained by the classic eigenvalue-eigenvector free vibration problem of the structure and, thus, depends on  $\mathbf{M}_{\mathbf{s}}$  and  $\mathbf{K}_{\mathbf{s}}$ :  $\boldsymbol{\Phi} = \boldsymbol{\Phi}(\mathbf{M}_{\mathbf{s}}, \mathbf{K}_{\mathbf{s}})$ . The structural damping  $\mathbf{C}_{\mathbf{s}}$  will be assumed null without loss of generality.

The FE elastic stiffness  $\mathbf{K}_{\mathbf{s}}$  and mass  $\mathbf{M}_{\mathbf{s}}$  matrices are modelled with beam finite elements, in addition to nonstructural elements (e.g. concentrated masses), and are obtained through the well-known procedure of *matrix assembly* starting from the contributions at *element* level. For example, the beam element matrices  $\mathbf{K}_{\mathbf{e}}$  will contribute to  $\mathbf{K}_{\mathbf{s}}$  as follows:

$$\mathbf{K}_{\mathbf{s}} = \sum_e \mathbf{L}_{\mathbf{e}}^T \mathbf{K}_{\mathbf{e}} \mathbf{L}_{\mathbf{e}} \quad (8)$$

where  $\mathbf{L}_{\mathbf{e}}$  is the rotation matrix relating the local nodal displacements and the global ones, and the  $\sum_e$  operation is adopted in its general meaning of assembly over all the finite elements [19]. In turn, the matrix  $\mathbf{K}_{\mathbf{e}}$  is a function of the local geometry and material properties, e.g., the Young modulus of the beam  $E$ , its moment of inertia  $I$ , and the beam length  $l$ .

As for the evaluation of unsteady aerodynamic forces, a Double Lattice Method (DLM) solver developed by the authors of reference [17] is used. Given a reduced frequency  $k$  (nondimensional counterpart of the dimensional frequency  $\omega$ ) and a set of  $n_s$  normal modes, the DLM tool evaluates, in the frequency domain, the GAF matrix  $\mathbf{Q}_{hh}(ik)$ . This matrix contains the transfer functions from generalized displacements  $\boldsymbol{\eta}$  to generalized aerodynamic forces normalized by the dynamic pressure  $q_{\infty}$  at the reduced frequency  $k$ . Since  $\mathbf{Q}_{hh}$  represents a transfer matrix between generalised quantities, it depends on the structural modes  $\boldsymbol{\Phi}$ , which are provided as input to the DLM code, and thus variations in the structural parameters do have an effect on the calculation of  $\mathbf{Q}_{hh}$ .

Another important remark is that  $\mathbf{Q}_{hh}$  does not have a rational dependence on  $k$ . Therefore, in order to build up a linear state-space formulation of Eq. (6), Rational Function Approximation (RFA) strategies are typically adopted [1]. In particular, the RFA method employed in this work is the so-called Roger's Approximation method [20]. According to this RFA approach, the GAF matrix is approximated as follows:

$$\mathbf{Q}_{hh}(ik) \cong \mathbf{A}^{\mathbf{Q}}(ik) = (ik)^2 \mathbf{A}_2^{\mathbf{Q}} + (ik) \mathbf{A}_1^{\mathbf{Q}} + \mathbf{A}_0^{\mathbf{Q}} + \sum_{L=3}^{N_Q} \frac{ik}{(ik) + \gamma_{L-2}} \mathbf{A}_L^{\mathbf{Q}} \quad (9)$$

where the matrices  $\mathbf{A}_i^{\mathbf{Q}}$  with  $i = 0, \dots, N_Q$  are coefficient matrices found by applying a linear least-square fitting to the aerodynamic operator  $\mathbf{Q}_{hh}(ik)$  over the considered set of reduced frequencies  $k$ , and  $\gamma_i$  are lag coefficients chosen by the user. In practice, the high-pass filters in (9) capture the memory effect of the wake, which results in a phase shift and magnitude change with respect to the instantaneous aerodynamic loads (or quasi-steady contribution, represented by the first part of the approximation).

### 2.3. Aeroelastic equation for LFT modeling

In [6] the application of the LFT paradigm to describe uncertain aeroelastic systems was discussed. Specifically, it was detailed how to derive LFT models starting from a description of the aeroelastic system provided in frequency-domain (Eq. 6) or in state-space. This distinction is relevant in the robust control community [2]. For example, the latter favours the usage of advanced robust analysis (e.g. Integral Quadratic Constraints [11]) and control design techniques [9]. Therefore, the starting point for LFT modeling will be formulated here in state-space and the corresponding representation will be derived in this section.

Based on the direct analytical continuation from reference [21], if an analytical function such as that of Eq. (9) is known in terms of the imaginary variable  $ik$ , the same expression can be used with a generic complex variable  $s = g + ik$  without loss of validity. Thus, the problem can be expressed in the  $s$  domain by just substituting in Eq. (6)  $ik$  with  $s$  and replacing the GAF matrix  $\mathbf{Q}_{hh}$  with the RFA from (9):

$$[s^2 \bar{\mathbf{M}}_s + s \bar{\mathbf{C}}_s + \bar{\mathbf{K}}_s - q_\infty \mathbf{A}^{\mathbf{Q}}(s)] \boldsymbol{\eta}(s) = 0 \quad (10)$$

where  $s$  is the (dimensionless) Laplace variable. The resulting state-space equations include augmented aerodynamic states  $\boldsymbol{\eta}_{aL}$  ( $L = 3, \dots, N_Q$ ) due to the RFA and can be explicitly written out as:

$$\begin{bmatrix} \dot{\boldsymbol{\eta}} \\ \ddot{\boldsymbol{\eta}} \\ \dot{\boldsymbol{\eta}}_{a3} \\ \vdots \\ \dot{\boldsymbol{\eta}}_{aN_Q} \end{bmatrix} = \begin{bmatrix} 0 & \mathbf{I} & 0 & \dots & 0 \\ -\hat{\mathbf{M}}^{-1} \hat{\mathbf{K}} & -\hat{\mathbf{M}}^{-1} \hat{\mathbf{C}} & q \hat{\mathbf{M}}^{-1} \mathbf{A}_3^{\mathbf{Q}} & \dots & q \hat{\mathbf{M}}^{-1} \mathbf{A}_{N_Q}^{\mathbf{Q}} \\ 0 & \mathbf{I} & -\frac{V_\infty}{L} \gamma_1 \mathbf{I} & \dots & 0 \\ \vdots & \vdots & \vdots & \ddots & \vdots \\ 0 & \mathbf{I} & 0 & \dots & -\frac{V_\infty}{L} \gamma_{N_Q-2} \mathbf{I} \end{bmatrix} \begin{bmatrix} \boldsymbol{\eta} \\ \dot{\boldsymbol{\eta}} \\ \boldsymbol{\eta}_{a3} \\ \vdots \\ \boldsymbol{\eta}_{aN_Q} \end{bmatrix} \quad (11)$$

$$\dot{\mathbf{x}} = \mathbf{A} \mathbf{x}$$

where  $\mathbf{A}$  is the state-matrix of the system,  $\mathbf{x} = [\boldsymbol{\eta} \ \dot{\boldsymbol{\eta}} \ \boldsymbol{\eta}_{aL}]^T$  and  $\hat{\mathbf{M}}$ ,  $\hat{\mathbf{C}}$  and  $\hat{\mathbf{K}}$  are respectively the generalized aeroelastic inertial, damping and stiffness matrices:

$$\begin{aligned} \hat{\mathbf{M}} &= \bar{\mathbf{M}}_s - \frac{1}{2} \rho_\infty b^2 \mathbf{A}_2^{\mathbf{Q}} \\ \hat{\mathbf{C}} &= \bar{\mathbf{C}}_s - \frac{1}{2} \rho_\infty b V_\infty \mathbf{A}_1^{\mathbf{Q}} \\ \hat{\mathbf{K}} &= \bar{\mathbf{K}}_s - \frac{1}{2} \rho_\infty V_\infty^2 \mathbf{A}_0^{\mathbf{Q}} \end{aligned} \quad (12)$$

Note that the focus of this work is on stability, hence only the state-matrix  $\mathbf{A}$  is reported in Eq. (11). Specifically, the flutter speed  $V_f$  is the lowest value of  $V_\infty$  for which  $\mathbf{A}$  has a pair of eigenvalues on the imaginary axis. In case the system has inputs (e.g. gust, control surfaces) and outputs (e.g. load factors), and also robust performance or control design are considered, the state-space model will comprise the four state-matrices  $[\mathbf{A} \ \mathbf{B}; \ \mathbf{C} \ \mathbf{D}]$  classically used to describe a Linear Time Invariant (LTI) system.

Finally, Fig. 1 shows a schematic description of the main components involved in the FSI problem.

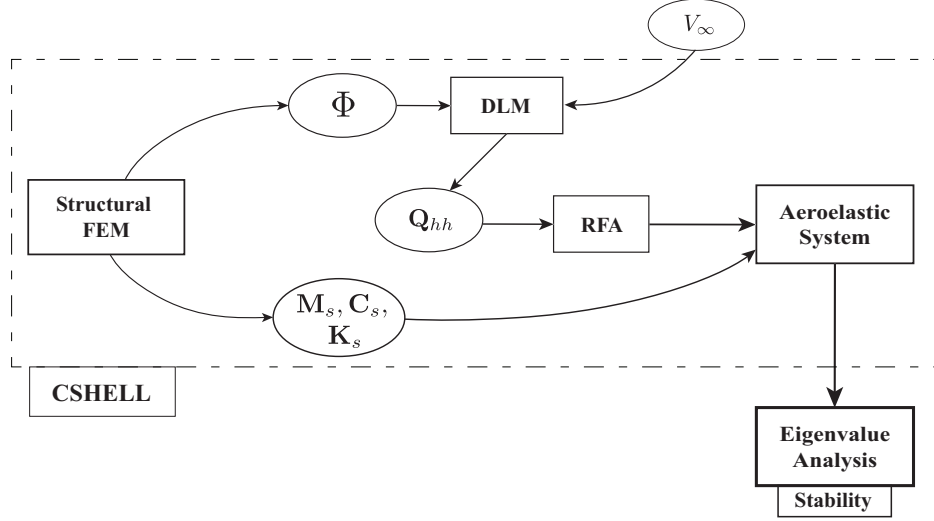


Figure 1: Sketch of CSHELL and of the flutter stability problem.

### 3. Numerical LFT approaches

The goal of this section is to first present the state-of-practice in LFT modeling of high-order aeroelastic systems and highlight the current limitations (Section 3.1). Strategies to mitigate these are then proposed in Section 3.2, where among others the concept of *modal-oriented* LFT approach is introduced. Notwithstanding the proposed improvements, inherent limitations hold for this approach to LFT modeling, as commented in Section 3.3. These reflections are fundamental to emphasize important aspects often neglected in the literature, and pave the way for the novel approach developed in Section 4.

#### 3.1. Overview of previous approaches proposed in the literature

The LFT modeling of high-order systems is commonly accomplished via numerical approaches. They are typically based on linearizing the high-fidelity model at scattered values of the parameters in the uncertainty set [22, 23], followed by a model-order reduction [7] to obtain lower-size LTI representations. The family of LTI systems is then interpolated so that a polynomial description is obtained. Finally, advanced algorithms which allow polynomial expressions to be recast into LFTs [24, 25, 26] are applied.

This approach has been applied already to aeroelastic systems in the last two decades. In [27] a systematic approach to perform the sequential operations described before was presented. It was shown that standard modal truncation cannot be employed as reduction technique because numerical and modal consistency problems can be encountered due to the complexity of the models. These issues compel employing model reduction strategies that achieve state vector consistency among the reduced LTIs. This consistency property is desirable so that the resulting polynomial interpolation exhibits regular modal trajectories and frequency responses with respect to the uncertain parameters, but it is not straightforward to achieve. A more sophisticated version was discussed in [7], where advanced reduced order algorithms were proposed specifically tailored to address the LFT nature of the final representation in the interpolation step. In both cases [27, 7], the accuracy of the LFT is only validated by comparing eigenvalues and frequency domain indicators (e.g. Bode plots), but no  $\mu$  flutter analysis is pursued. Thus, there was no validation of the results in terms of worst-case perturbations and resulting flutter speeds with respect to the original high-order system.

This type of validation was addressed in [8], which showed that the robust predictions aided in the comprehension of nonlinear phenomena observed during flight. However, only a small number of uncertainties was considered and there was no mention of systematic approaches to deal with broader uncertainty sets.

In view of the scenario described above, it is deemed relevant to develop LFT modeling methodologies capable of addressing present restrictions and limitations. Starting from the class of numerical approaches, possible improvements are discussed in Section 3.2.

### 3.2. Improved construction of numerical LFTs

The proposed methodology consists of distinct approaches for the structural and aerodynamics uncertain operators.

For the structural uncertainty case, once the corresponding set  $\Delta$  is defined, an appropriate number of samples  $n_{pts}$  must be selected. A good initial guess is represented by the vertices of the set, i.e. all the possible combinations of the extreme values of the uncertainties. For cases with a large number of uncertainties this will be prohibitively large, i.e.  $n_{pts}=2^{n_{str}}$  where  $n_{str}$  is the number of independent parameters in  $\Delta$ . In these cases it might be necessary to perform a sensitivity analysis and apply as well engineering judgment to reduce the number of samples.

For each sample, the structural solver is run and the generalized modal operators  $\bar{\mathbf{M}}_{\mathbf{s}}$  and  $\bar{\mathbf{K}}_{\mathbf{s}}$  from Eq. (7) are evaluated. This leads to a family of matrices  $\bar{\mathbf{M}}_{\mathbf{s}}(\Delta)$ ,  $\bar{\mathbf{K}}_{\mathbf{s}}(\Delta)$  which are interpolated in order to find polynomial expressions describing the dependence of the modal operators on the parameters of the set. In this work, this step is performed by means of the APRICOT library [28] of the SMAC toolbox. This library offers a wealth of routines to perform the polynomial interpolation more efficiently than the classically employed least-square method. The routine used here is *olsapprox*, which implements an orthogonal least-square method that allows obtaining a multivariate sparse polynomial approximation for the coefficients of the matrices. Sparsity is a highly advantageous feature since it alleviates the issue of data overfitting and it has the benefit to minimize the size of the resulting LFT. The algorithm allows the definition of a threshold on the maximum error of the interpolation (checked via a comparison with all the samples provided as input) and the degree of the approximant. Finally, the polynomial matrices are converted into LFTs and the state-space representation of the system (Eq. 11) is built up.

An important feature of the methodology proposed here is that the interpolation is applied separately to the modal operators (i.e.  $\bar{\mathbf{M}}_{\mathbf{s}}$  and  $\bar{\mathbf{K}}_{\mathbf{s}}$ ) instead of directly to the state-matrix  $\mathbf{A}$ . This is referred here as *modal-oriented* LFT modeling approach, to stress that the LFT transformation is applied to the distinct modal operators, rather than to the final state-matrix as typically done [7]. It is also noted that the advantage of building LFT models starting from specific *building blocks* of the dynamics rather than directly from the state-space equation has been already recognized in the community [25, 24, 8]. The advantageous features of this approach are discussed next.

Since it interpolates directly modal quantities, this algorithm automatically provides state vector consistency among the different interpolated operators, which in previous applications have proved to require an additional step. Regarding this, the numerical problems encountered in [27] are not an issue with this approach because the modal content is discerned at the structural operator level, and not at the aeroelastic one (Eq. 11) where aerodynamic coupling makes it more difficult. A further advantage is that it is possible to generate different LFTs, each differing in the number of modes  $n_{\delta}$  affected by uncertainties (with  $n_{\delta} \leq n_s$ , where  $n_s$  is the number of modes retained in the modal decomposition). This allows identifying the minimum number of modes where uncertainties have to be introduced to obtain a valid flutter analysis result and, by doing so, can provide a lower size aeroelastic LFT model to be employed in subsequent extensive robust analyses (e.g. the  $\mu$  sensitivity analyses commented in [5]). Moreover, the possibility to consider different  $n_{\delta}$  in the analyses can provide further insight into the instabilities affecting the system. Finally, this method allows the structure of the aeroelastic equation (11) to be exploited when performing the numerical approximation. This helps to further reduce the size of the LFT compared to the case where all the terms of the state-matrix are interpolated.

With respect to the case of uncertainties related to the aerodynamic operator, it must be noted that the sources of uncertainty can be ascribed to different causes. For example: variations in structural parameters not (accurately) taken into account; simplifying modeling assumptions (e.g. potential flow); and numerical



approximations (e.g. calculation of  $\mathbf{Q}_{hh}$  on a discrete set of frequencies or rational fitting of  $\mathbf{A}^{\mathbf{Q}}$ ).

With regard to the first of the sources of uncertainty, recall from the definition of the aerodynamic operator in Section 2.2 that perturbations in the structural operators lead to changes in  $\mathbf{Q}_{hh}$ . In principle, this can be tackled as for the structural operators, i.e. generating a polynomial interpolation of the state-space operator  $\mathbf{A}^{\mathbf{Q}}$  (Eq. 9). However, this entails evaluating samples of  $\mathbf{Q}_{hh}$  (at different frequencies) and performing a polynomial interpolation of the rational approximants, which could be computationally demanding. Alternatively, a frequency-domain characterization of the associated error can be estimated and based on this the aerodynamic uncertainty description can be formulated using the method proposed in [6]. The fundamental idea is to express the uncertainties directly in the original frequency domain operator  $\mathbf{Q}_{hh}$  despite the fact that the system is formulated in state-space (Eq. 11). This approach privileges a physics-driven definition of the uncertainties because it allows to work with the transfer matrix between displacements and loads. This is achieved by means of a particular application of the concept of unmodelled dynamics in the context of aeroelastic operators [2]. Note first that, since the GAF matrix provides a relation between displacements (but not speeds or accelerations) and loads, only the aeroelastic stiffness matrix  $\hat{\mathbf{K}}$  has to be considered. This matrix, recall its definition in Eq. (12), can thus be written as:

$$\hat{\mathbf{K}} = \bar{\mathbf{K}}_s - \frac{1}{2}\rho_{\infty}V_{\infty}^2\mathbf{A}_0^{\mathbf{Q}} - \mathbf{V}_{\mathbf{Q}}\Delta_{\mathbf{Q}}\mathbf{W}_{\mathbf{Q}} \quad (13)$$

The nominal part of the aeroelastic stiffness matrix (i.e. the first two terms in the right hand side) is given by the state-space model, while the uncertainty part employs a standard description of the uncertainty (4) with scaling matrices (potentially frequency dependent)  $\mathbf{V}_{\mathbf{Q}}$  and  $\mathbf{W}_{\mathbf{Q}}$  and structured complex matrix  $\Delta_{\mathbf{Q}}$  containing the uncertainty in the transfer functions of  $\mathbf{Q}_{hh}$ . This representation at operator level provides, at LFT level, the expression for  $\mathbf{M}$  used by  $\mu$  for the robust stability test (5). The reader is referred to [6] for more technical details on the derivation of this uncertainty description.

Compared to standard approaches in the literature, which apply uncertainties in the approximated aerodynamic matrices forming  $\mathbf{A}^{\mathbf{Q}}$  (e.g. in [3] uncertain lag roots are analysed), this method allows the uncertainty definition to be assisted by physical considerations. For instance, if a lack of accuracy (based on the evidence of experimental results or other computational data) is detected in some of the transfer functions of  $\mathbf{Q}_{hh}$ , it is then possible to model it directly as an additional uncertain parameter. Moreover, the matrix coefficients in  $\mathbf{Q}_{hh}$  are complex and so are the associated uncertainties, resulting in a notable improvement on the accuracy and run time of the  $\mu$  analyses [2].

Application of this numerical LFT-FSI modeling approach for the analysis of one of the case studies is presented in Section 5.2.

### 3.3. Assessment of issues in numerical LFT approaches

The uncertainty modeling approach discussed in Section 3.2 features improvements with respect to standard approaches, but some drawbacks can be observed in relation with: i) the accuracy of the LFT as a result of the polynomial interpolation, ii) the allowed uncertainty descriptions, and iii) computational efficiency. These aspects will be further discussed next.

Since the proposed approach relies on a polynomial interpolation, the accuracy of the numerical LFT depends on the uncertainty set considered. This can be shown using the example of Fig. 2 where the subdivision in  $N$  stations of a notional wing is depicted. Each of these regions can be thought of as the variable space of the structural uncertain parameters that can be exploited to obtain by design a better flutter behavior for the system. From the system optimization perspective, it is natural to aim at considering a description characterized by, with reference to Fig. 2, a refined stations' grid (large  $N$ ) with localized, concentrated masses at each wing station (small  $\delta_{M_i}$ ).

This uncertainty description might prove to be challenging when the numerical LFT approach is pursued. The selection of a large number of uncertain parameters with very localized uncertainty values and ranges might indeed hinder the effectiveness of the LFT modeling, but also of the subsequent  $\mu$  analysis, algorithms. The ensuing interpolation can indeed: be inaccurate (e.g. small variations in localized uncertainties might not be well captured; or a large number of uncertainties might force to consider a coarse parametric grid);

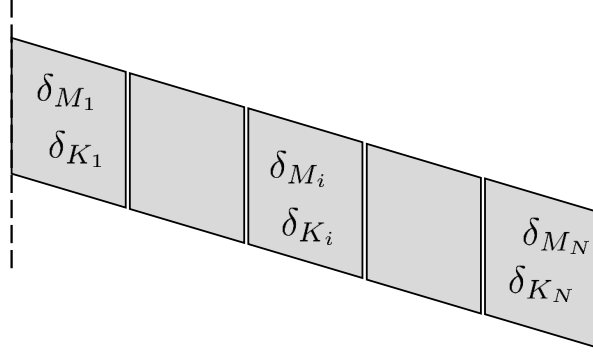


Figure 2: Schematic uncertainty description of a notional aircraft wing (view from the top).

lead to intractable LFTs (due to the  $\Delta$ -block size); or be computationally intensive (due to the large number of samples to be computed with the FSI solver). This is indirectly confirmed by examples from the literature [8, 27, 7], where a maximum of three parameters were considered, all representing large quantities (e.g. extreme filling levels of the fuel tanks).

As for the computational aspects, in addition to what was said before, note that the numerical LFT approach must be performed anew for any change in the model, and this could be particularly computationally expensive depending on the density of the parametric grid.

#### 4. A novel LFT-FSI co-modeling framework

The limitations observed in Section 3 with respect to numerical LFT approaches prompted the research for alternative LFT modeling strategies. In [3] (a foundational contribution to the  $\mu$ -flutter topic) the uncertainty description is done by introducing a posteriori (and thus avoiding the interpolation) parametric uncertainties in the generalized structural matrices of Eq. (7) as well as in the approximated aerodynamic matrices (Eq. 9). This is a practical way of building LFTs, but the reconciliation between physical sources of uncertainty and LFT parameters is more difficult. A similar approach was taken in [4] for the structural operators, whereas a physical description of the aerodynamic uncertainties directly applied to the GAF matrix was proposed. This was however limited to systems described in the frequency-domain (Eq. 6).

It is thus considered of interest the development of an alternative LFT formulation which aims at addressing the issues discussed above, with particular emphasis on structural parametric uncertainties. Note that, for the aerodynamic uncertainties case, the solution from [6] commented in Section 3.2 retains already the desired features discussed here.

##### 4.1. A symbolic LFT-FSI modeling algorithm

The previous discussion prompts the idea of performing the LFT modeling task at *FSI solver level*. By this, it is meant here that the uncertain parameters are introduced in the structural solver when the high-fidelity operators are assembled (as described in Section 2.2). The steps entailed by this symbolic modeling algorithm are listed in Algorithm 1, whereas Fig. 3 presents the approach by means of a flow chart.

---

**Algorithm 1** Symbolic co-modeling algorithm's pseudocode

---

**Input:** nominal model, uncertainty set  $\Delta$ , modal matrix  $\Phi$

**Output:** aeroelastic LFT  $\mathcal{F}_u(\bullet, \Delta)$

- 1: **Define** symbolic parameters associated to the elements of  $\Delta$  (Step-S1)
  - 2: **Assemble** the symbolic physical matrix inside the structural solver (Step-S2)
  - 3: **Compute** the symbolic modal matrices using  $\Phi$  (Step-S3)
  - 4: **Build** an LFT representation of the symbolic modal matrices (Step-S4)
  - 5: **Compute** the aerodynamic operators using  $\Phi$
  - 6: **Build** an LFT representation of (11) (Step-S5)
- 

As an example, let us consider the structural mass matrix  $\mathbf{M}_{\mathbf{B}_j}$  of the beam  $j$  which, in a similar fashion as described in Section 2.2 for  $\mathbf{K}_e^B$ , will contribute to the corresponding structural matrix (in this case  $\mathbf{M}_s$ ):

$$\mathbf{M}_{\mathbf{B}_j} = \begin{bmatrix} \mathbf{M}_{\mathbf{tt}} & \mathbf{M}_{\mathbf{tr}} \\ \mathbf{M}_{\mathbf{tr}} & \mathbf{M}_{\mathbf{rr}} \end{bmatrix} \quad \begin{aligned} \mathbf{M}_{\mathbf{tt}} &= \mathbf{F}_1(L_j, m_j, I_{z_j}, I_{y_j}) \\ \mathbf{M}_{\mathbf{tr}} &= \mathbf{F}_2(L_j, m_j, I_{z_j}, I_{y_j}) \\ \mathbf{M}_{\mathbf{rr}} &= \mathbf{F}_3(L_j, m_j, I_{z_j}, I_{y_j}) \end{aligned} \quad (14)$$

where the subscripts  $t$  and  $r$  refer to translational and rotational degrees of freedom. The parameters  $L_j$ ,  $m_j$ ,  $I_{z_j}$ , and  $I_{y_j}$  are respectively the beam length, mass and moments of inertia, while  $\mathbf{F}_1$ ,  $\mathbf{F}_2$ , and  $\mathbf{F}_3$  are polynomial matrix functions of these properties. When some of these parameters are considered uncertain and thus the functions are not evaluated at the corresponding nominal values, the local physical operator  $\mathbf{M}_{\mathbf{B}_j}$  is a matrix function of the uncertainties. If the parameters are defined as symbolic objects (Step-S1),  $\mathbf{M}_{\mathbf{B}_j}(\Delta(\delta_{j-\bullet}))$ , with  $\bullet = L, m, I_z, I_y$ , is a symbolic operator that will contribute to the structural mass matrix  $\mathbf{M}_s$  (Step-S2). This step is general and can be applied to other contributions to the mass operator (e.g. concentrated masses) and to other operators (e.g. stiffness).

Once the *symbolic* physical matrices are obtained with the procedure outlined before, a modal truncation is performed (Step-S3):

$$\begin{aligned} \bar{\mathbf{M}}_s(\Delta) &= \Phi^T \mathbf{M}_s(\Delta) \Phi \\ \bar{\mathbf{C}}_s(\Delta) &= \Phi^T \mathbf{C}_s(\Delta) \Phi \\ \bar{\mathbf{K}}_s(\Delta) &= \Phi^T \mathbf{K}_s(\Delta) \Phi \end{aligned} \quad (15)$$

where  $\Delta$  indicates the uncertainty set gathering the symbolic parameters –the selection of the modal matrix  $\Phi$  will be discussed in the next subsection. Given the symbolic modal matrices  $\bar{\mathbf{M}}_s$ ,  $\bar{\mathbf{C}}_s$ , and  $\bar{\mathbf{K}}_s$ , it is possible to apply standard LFT algorithms [24] which allow polynomial matrices to be recast into the formalism of Eq. (2). In this way, the modal LFTs  $\mathcal{F}_u(\bar{\mathbf{M}}_s, \Delta)$ ,  $\mathcal{F}_u(\bar{\mathbf{C}}_s, \Delta)$ ,  $\mathcal{F}_u(\bar{\mathbf{K}}_s, \Delta)$  are obtained (Step-S4). The final step consists in building up the aeroelastic LFT (Step-S5). This can be done by substituting the modal LFTs and the aerodynamic operator (function also of  $\Phi$ ) in the state-space model (11).

The implementation of the LFT modeling *inside* the FSI solver can be regarded as a nontrivial aspect of this approach. To begin with, the development of an LFT-FSI methodology requires a close alignment between the modeling paradigms used by each corresponding community, i.e. the robust control and the aeroelastic. Thus, it requires tight collaboration, and a certain level of mutual understanding, between experts from the two disciplines. In addition to that, the handling of symbolic objects represents an aspect worth mentioning. If, as in this case, the FSI solver is available in MATLAB®, the uncertain physical parameters can be defined as symbolic objects in Step-S1 by means of the Symbolic Math toolbox [29]. With reference to Fig. 3, this allows to work in Step-S2 and Step-S3 with symbolic objects and then, by means of the LFR toolbox [24], convert them into LFTs (Step-S4). This toolbox allows to handle LFTs in an efficient fashion by means of LFR objects, which are used also for the aeroelastic LFT (Step-S5) and finally provides a representation of the system which is suitable for the application of  $\mu$ . However, the method discussed in this section can in principle be applied also when the FSI solvers are implemented using other coding languages, thus the implementation aspects should not be regarded as a limitation. For example

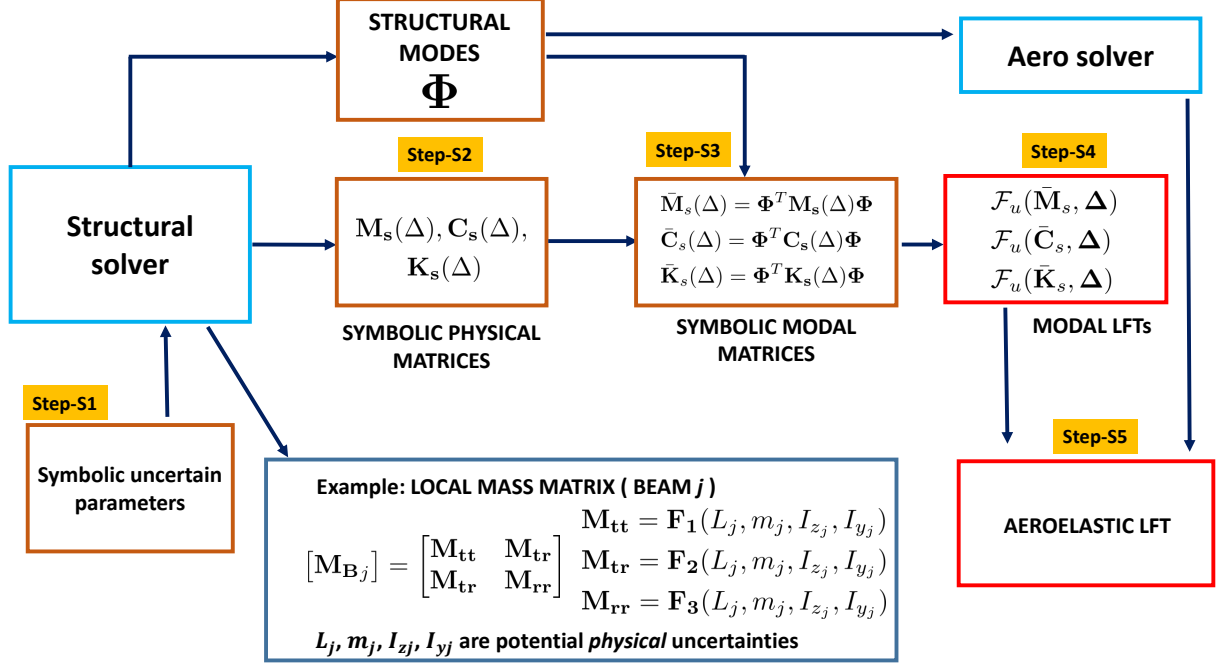


Figure 3: Symbolic LFT co-modeling algorithm's chart.

FORTTRAN-based codes have been interfaced with symbolic computational languages (e.g. MAPLE) to provide computationally efficient framework for LFT modeling [30].

A crucial aspect of this formulation is the handling of the modal matrix  $\Phi$ . First, it should be noted that many of the approaches to structural uncertainty descriptions assume for the robust analyses a fixed modal base (typically the one corresponding to the nominal system) [3, 8, 31, 4]. This is an approximation and potentially a source of error since  $\Phi$  is also altered when there are structural uncertainties in  $\Delta$ .

Different solutions have been proposed by the community. In [32] it was proposed a first-order dependence of the structural modes on the uncertain parameters based on the application of perturbation theory. This strategy is appealing since it allows the modal matrix to be expressed analytically as a function of the uncertainties, i.e.  $\Phi(\Delta)$ . However, it also presents important drawbacks as commented in [33], where different approaches to tackle the modal bases selection were discussed. For example, the perturbed modal base approach is deemed the most computationally expensive among them due to the resulting LFT size, and the linear modal shapes variation hypothesis is shown to be erroneous, even for relatively simple wing geometry layouts, as the structural uncertainties ranges increase. Higher order Taylor expansions can be considered, but the overall LFT size grows significantly, making the  $\mu$  calculation problem numerically intractable or compromising its accuracy. An interesting idea discussed in [33] consists in updating the modal base with the worst-case perturbations obtained by  $\mu$ . This represents the premise of the approach taken in this work to overcome the issue related to  $\Phi$ , and will be detailed in Section 4.2.

Note first that, when the operation in Eq. (15) is performed, the obtained symbolic modal matrices are generally full. This is a source of error related to the fixed modal base-assumption, because due to eigenvectors properties, the modal mass and stiffness matrices are always diagonal. That is, regardless of the specific perturbation matrix affecting the system, the perturbed modal matrices will be diagonal. By leveraging the facts that LFTs are built at FSI solver level with a modal-oriented approach, this inaccuracy

can be eliminated a priori by retaining, at Step-S3 in Fig. 3, only the diagonal terms of the matrices:

$$\begin{aligned}\bar{M}_s(\Delta) &\equiv \text{diag}(\Phi^T M_s(\Delta) \Phi) \\ \bar{C}_s(\Delta) &\equiv \text{diag}(\Phi^T C_s(\Delta) \Phi) \\ \bar{K}_s(\Delta) &\equiv \text{diag}(\Phi^T K_s(\Delta) \Phi)\end{aligned}\tag{16}$$

As a result, the error due to the modes is reduced and confined only to the diagonal terms.

While this modification of Step-S3 allows to mitigate and confine the error in the symbolic modal matrices to the diagonal terms, the fixed modal base assumption can still lead to wrong predictions. For example, the effect of perturbations in  $\Phi$  on the aerodynamic operator must still be addressed. The analysis algorithm proposed in the next section overcomes this issue.

#### 4.2. A symbolic LFT-FSI $\mu$ analysis algorithm

This section proposes an iterative analysis algorithm complementing the symbolic modeling approach presented in Section 4.1. The aim of Algorithm 2 is to determine (if it exists) a worst-case perturbation  $\hat{\Delta}^{cr}$ , associated with the LFT built with the symbolic approach, that makes the system flutter at a speed  $V_\mu$  chosen by the user. The key feature in order to achieve accurate results is represented by the update of the modal matrix used in Step-S3 of Algorithm 1, where the transformation from symbolic physical matrices into symbolic modal matrices takes place. This is performed iteratively, as reported in the associated pseudocode and schematically illustrated in Fig. 4.

The algorithm requires the symbolic physical matrices  $\mathbf{M}_s(\Delta)$ ,  $\mathbf{C}_s(\Delta)$ , and  $\mathbf{K}_s(\Delta)$  from Step-S2 of Algorithm 1 (these are provided as input), which are held fixed throughout the iterations. The process is then started by initializing the modal base with  $\Phi_0$ . This allows to build the aeroelastic LFT (Step-A1) and a standard  $\mu$  analysis can thus be performed (Step-A2). The perturbation matrix  $\Delta^{cr}$  is extracted from the highest peak of the lower bound  $\mu_{LB}$ , and based on it the associated flutter speed  $V_{f\mu}$  can be calculated using the FSI solver (Step-A3). If the difference between  $V_{f\mu}$  and the perturbed flutter speed  $V_\mu$  is greater than the given tolerance  $\epsilon_V$ , the modal base is updated with the matrix  $\Phi^{cr}$  corresponding to  $\Delta^{cr}$  (Step-A4) and a new iteration is performed. Otherwise, a worst-case perturbation  $\hat{\Delta}^{cr}$  has been determined and from it (recall that by definition  $\mu = 1/\sigma(\Delta^{cr})$ ) the system robustness can be assessed. It is stressed the difference between  $\Delta^{cr}$  and  $\hat{\Delta}^{cr}$ . The former is provided by the  $\mu$ -lower bound computation at a generic iteration and, due to the modal base error, might not correspond to a flutter speed equal to  $V_\mu$ . The latter instead determines a flutter speed  $V_{f\mu} \approx V_\mu$  within given tolerance and thus is the sought worst-case perturbation.

---

#### Algorithm 2 Iterative algorithm for the worst-case perturbation

---

**Input:**  $V_\mu$ , symbolic physical matrices, nominal modal matrix  $\Phi_0$ , tolerance  $\epsilon_V$   
**Output:** worst-case perturbation  $\hat{\Delta}^{cr}$  such that  $V_\mu$  is the flutter speed  
**while**  $|V_\mu - V_{f\mu}| < \epsilon_V$   
1:  $\Phi \leftarrow \Phi_0$   
2: **Apply** Algorithm 1 from Step-S3 (Step-A1)  
3: **Compute**  $\mu$  using the aeroelastic LFT  $\mathcal{F}_u(\bullet, \Delta)$  from Step-A1 (Step-A2)  
4: **Extract**  $\Delta^{cr}$  (associated with the highest peak of  $\mu$ ) and compute  $V_{f\mu}$  (flutter speed of the perturbed system) in the FSI solver (Step-A3)  
5: **Check** optimality of the worst-case perturbation (optional)  
6: **Compute** the matrix  $\Phi^{cr}$  (Step-A4) and update  $\Phi_0 \leftarrow \Phi^{cr}$   
**return**  $\hat{\Delta}^{cr}$

---

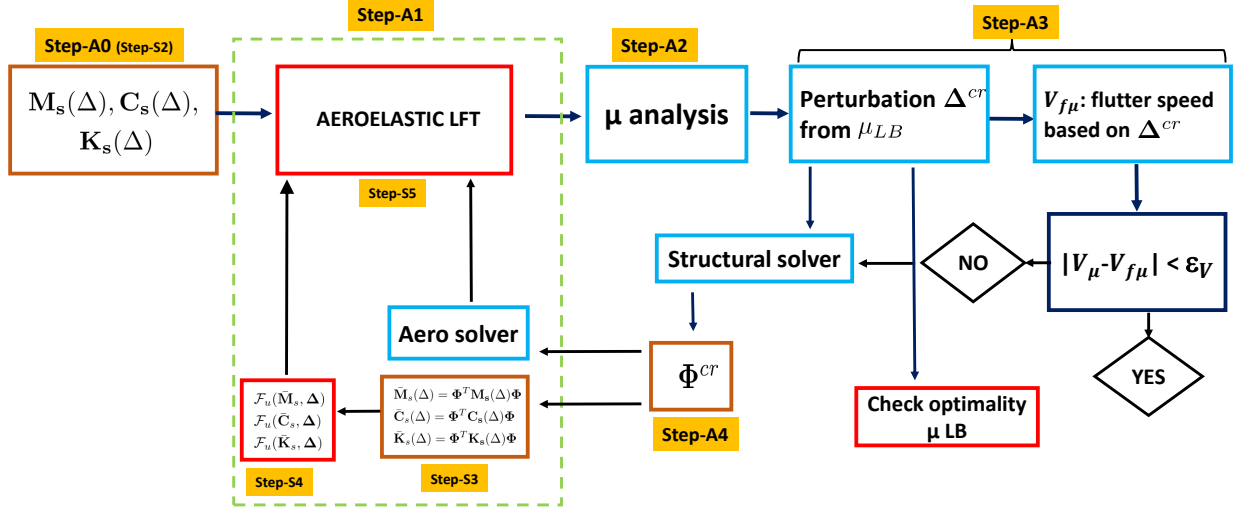


Figure 4: Iterative scheme block diagram.

To interpret the rationale underlying the analysis algorithm from an LFT perspective, the uncertain aeroelastic description achieved at Step-S5 of the modeling algorithm is expressed as follows:

$$\mathcal{F}_u(\mathbf{M}, \Delta) = \mathbf{M}_{22}(\Delta) + \mathbf{M}_{21}(\Delta)\Delta(\mathbf{I} - \mathbf{M}_{11}(\Delta)\Delta)^{-1}\mathbf{M}_{12}(\Delta) \quad (17)$$

Eq. (17) reflects the fact that it is not possible to express the effect of the uncertainties on  $\Phi$  in the standard linear fractional fashion used in LFT modeling. Crucially, when compared to the definition of LFT given in Eq. (2), the  $\Delta$  block affects here also the partitioned matrix  $\mathbf{M}$ . This clearly would not allow to apply  $\mu$  analysis, which requires an uncertain system described as a standard LFT. Indeed, the iterative scheme outlined in Fig. 4 proceeds by updating the matrix  $\mathbf{M}$  with the value of  $\Delta^{cr}$  given at the last iteration:

$$\mathcal{F}_u(\mathbf{M}, \Delta) \approx \mathbf{M}_{22}(\Delta^{cr}) + \mathbf{M}_{21}(\Delta^{cr})\Delta(\mathbf{I} - \mathbf{M}_{11}(\Delta^{cr})\Delta)^{-1}\mathbf{M}_{12}(\Delta^{cr}) \quad (18)$$

where at the first iteration  $\Delta^{cr} = 0$  is used, i.e. the nominal modal matrix  $\Phi_0$  is employed.

It is important to stress that the algorithm is based on the calculation of the lower bound, which is the result of a nonconvex optimization problem [2]. In addition, it is well known that for LFTs of large dimension and/or many parameters, the  $\mu_{LB}$  might be conservative (i.e. distant from the upper bound). This trend can be ameliorated with improved lower bound algorithms [34] or with recently developed  $\mu$  solvers which compute  $\mu_{UB}$  and  $\mu_{LB}$  together ensuring they hold values within a certain tolerance [35]. The latter library has been used in this work to assess the accuracy of the lower bound, but the algorithms are computationally demanding and thus, at least for the LFTs used in this work, it is not practical to embed them in the proposed iterative cycle.

For all these reasons, convergence to the global optimum (i.e. the matrix  $\hat{\Delta}^{cr}$  with the smallest magnitude) of the solution found with the iterative algorithm cannot be mathematically guaranteed. In order to highlight this,  $\hat{\Delta}^{cr}$  has been termed “a” worst-case perturbation matrix. In other words, even if the converged  $\hat{\Delta}^{cr}$  leads to a flutter speed equal (within the prescribed tolerance) to  $V_\mu$ , there could be another one  $\hat{\Delta}_{glob}^{cr}$  with  $\bar{\sigma}(\hat{\Delta}_{glob}^{cr}) < \bar{\sigma}(\hat{\Delta}^{cr})$ . In addition to the numerical issues mentioned above, failure in converging to the global optimum can be ascribed to the rule with which the modal matrix  $\Phi$  is updated. Therefore, strategies to qualitatively check the optimality of the lower bound at each iteration are introduced now.

First, the *directionality* of the worst-case is monitored. This entails observing at each iteration the sign change from the predicted perturbation for each of the uncertain parameters. If this remains the same, it is reasonable even though not rigorous, to argue that the worst-case perturbation for that parameter is

detected. Moreover, when this pattern is observed robustness properties such as sensitivity of flutter to certain parameters [5] can be inferred based on analyses which use the nominal modal matrix  $\Phi_0$ . For those parameters whose sign (or magnitude) changes, it is advisable to perform a flutter sensitivity analysis, since the discontinuity could be ascribed to the small importance of that parameter for the instability.

A second strategy, which complements the previous assessments, is represented by Algorithm 3, schematically depicted in Fig. 5, which can be applied in principle at the end of each iteration (in practice, a trade-off with computational efficiency will arise). The algorithm takes as input the worst-case matrix  $\Delta^{cr}$  computed at Step-A3 of a generic iteration of Algorithm 2 and aims at assessing its optimality (meant here as its proximity to the actual worst-case). First,  $N_c$  potential worst-case perturbations  $\Delta_i^t$  (with  $i = 1, \dots, N_c$ ) having all the same maximum magnitude  $\bar{\sigma}(\Delta^{cr})$  are defined (Step-C1). These definitions can be informed: by the directionality tests on the  $\Delta^{cr}$  at different iterations (e.g. changing the values for those parameters having a discontinuous behaviour), by available insights on certain critical parameters (e.g. from sensitivity analysis), or by considering opposite perturbations for some of the parameters, e.g.  $\Delta_i^t = -\Delta^{cr}$  if the sign of all parameters is changed. Note that the idea of testing far away from the *current best* is a known strategy in applied optimization. For example, in [36] a hybrid algorithm was proposed which crosses an evolutionary (global) optimizer with a local one, initialising the latter with either the best candidate in the population or those far away from the current best, depending on the improvement of the cost function. In this work, the population is represented by the set of selected  $\Delta_i^t$  and the same idea of exploiting domain knowledge to define it can be employed.

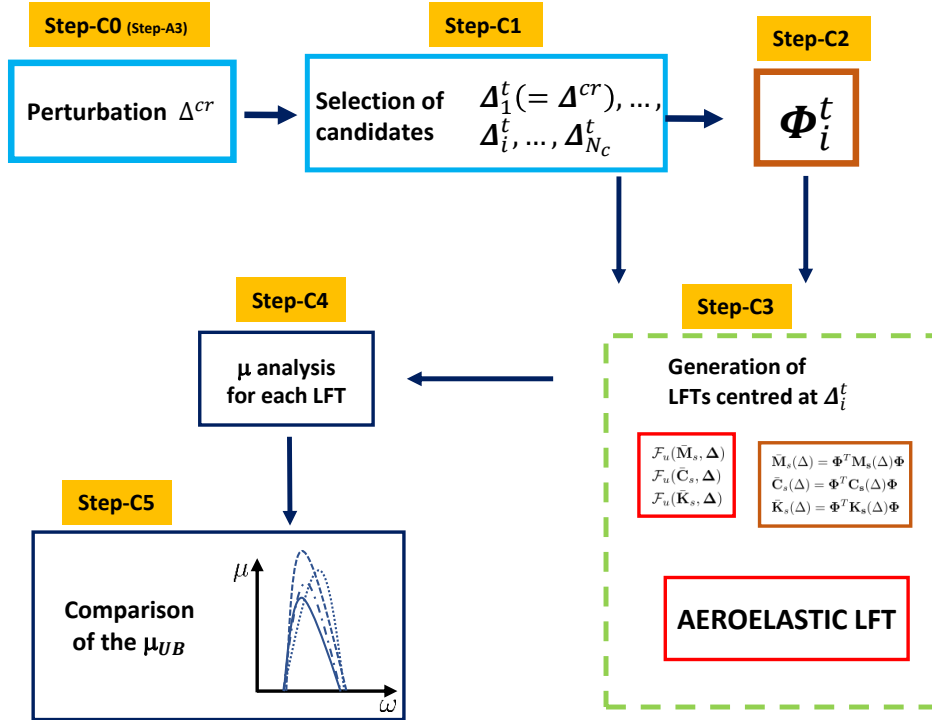


Figure 5:  $\mu_{UB}$ -based algorithm to check the optimality of the predicted worst-case.

---

**Algorithm 3** Algorithm to check optimality of the predicted worst-case

---

**Input:** critical perturbation  $\Delta^{cr}$  (from Step-A3 of Algorithm 2)

**Output:**  $\mu_{UB}$ -based assessment of the optimality of the worst-case

- 1: **Select**  $N_c$  perturbation matrices  $\Delta_i^t$  ( $i = 1, \dots, N_c$ ) (Step-C1)
  - 2: **Compute** the modal matrices  $\Phi_i^t$  associated with  $\Delta_i^t$  (Step-C2)
  - 3: **Use**  $\Phi_i^t$  to build  $N_c$  aeroelastic LFTs centered at  $\Delta_i^t$  (i.e. the parameters in  $\Delta_i^t$  are the nominal values for the uncertainties) (Step-C3)
  - 4: **Compute**  $\mu_{UB}$  for each LFT generated at the previous step (Step-C4)
  - 5: **Compare** the peaks  $\mu_{UB}^i$  of the curves and assess the optimality of  $\Delta^{cr}$  (Step-C5)
- 

In Step-C2 the modal matrices  $\Phi_i^t$  corresponding to each  $\Delta_i^t$  are computed, and subsequently  $N_c$  aeroelastic LFTs centered at each of the worst-case candidates are constructed (Step-C3). Note that the core idea is to compute each LFT using the relative modal basis  $\Phi_i^t$ . Then,  $\mu$  analysis is applied to each of these LFTs (Step-C4), focusing on the upper bounds  $\mu_{UB}$  since this is typically computed with convex programs. The peaks  $\mu_{UB}^i$  of each curve are employed as a measure of the proximity of the perturbed system  $i$  to the actual worst-case of the problem (Step-C5). Specifically, perturbations associated to larger  $\mu_{UB}^i$  point at worst-case directions, and thus this strategy can be used to verify that throughout the iterations the actual worst-case is detected.

## 5. Application to the Joined Wings aircraft

The LFT-FSI modeling approaches presented in the two previous sections are applied here to two joined-wing aircraft case studies. These are first presented in Section 5.1, where nominal (i.e. without considering uncertainty in the system) flutter analysis is also briefly commented.

In Section 5.2 robust analyses are carried out using the numerical LFT approach. An important outcome is that by exploiting the modal-oriented LFT modeling, the effect of perturbations on different modes can be captured, and from this interesting physical insights can be gained. However, the drawbacks anticipated in Sec. 3 are confirmed, especially with respect to the number and type of uncertain parameters that can be reliably captured in the LFT with this modeling approach. Section 5.3 presents the results obtained with the symbolic LFT approach, which confirm the favourable features described in Section 4. The modeling and analysis algorithms are shown to provide accurate predictions of the worst-case flutter speed of the wing in the face of the given uncertainty set. Importantly, the latter consists of a very fine mass and stiffness parameters distribution across the wing, which, to the best of the authors' knowledge, has never been considered so far in robust flutter analysis with analytic worst-case methods. This, together with the success of the Algorithm 3 in driving the analysis towards global minima (to these results is devoted Section 5.3.2), supports the main message conveyed here that the newly proposed co-modeling approach can represent a valuable tool in robustness analysis of high-order aeroelastic systems.

### 5.1. Joined-wing aircraft configurations

The analyzed system consists of a PrandtlPlane configuration (a particular case of Joined Wings [14], see Fig. 6). The only difference between the two case studies is that the first one features fuselage's inertia and flexibility, while the second one considers a clamped wing system (i.e. the presence of the fuselage is neglected).

#### 5.1.1. Case study 1: Wing plus elastic Fuselage (WF)

The unconventional PrandtlPlane was originally studied in [13]. The configuration, denominated PrandtlPlane 250 (PrP250) is a 250 passenger mid-long range (6000 nm) aircraft with a Maximum Take Off Weight of 230 tons, and was designed by considering a multidisciplinary approach. A view of the finite element (FE) model of the wing is given in Fig. 7. The fuselage is modeled as a beam, whose properties have been extrapolated and scaled back from the work in [38]. This case study is an evolution of that considered in [18] where only the fuselage inertial effects were retained.



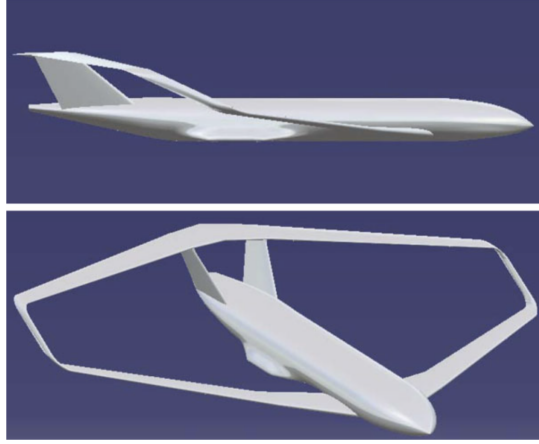


Figure 6: PrandtlPlane 250-seat concept, taken from [37].

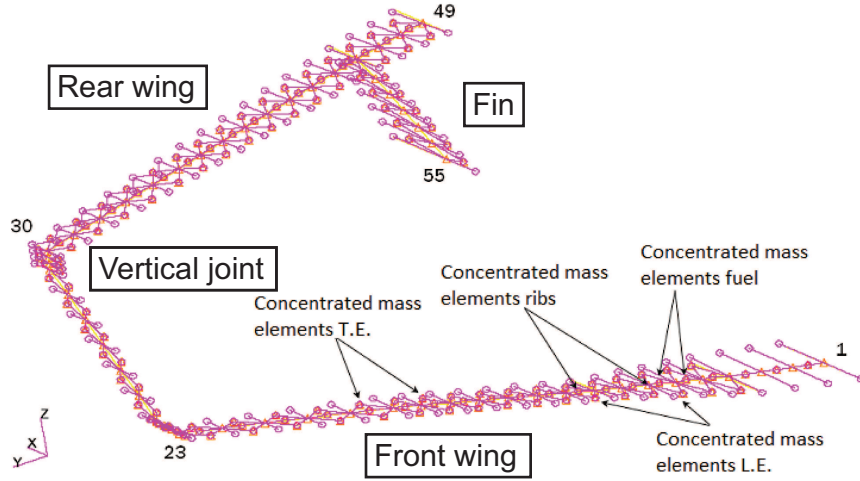


Figure 7: Structural model of the wing, taken from [13].

Fig. 8 shows the results of nominal flutter analysis in terms of frequency and damping of the poles of the system as a function of speed. The analyses have been carried out with CSHELL, and then validated with the commercial software NASTRAN [39]. Flutter occurs at approximately  $V_f = 270 \frac{m}{s}$  due to mode III. Additional instabilities, occurring at higher speeds, are determined by the coalescence of modes I-II and modes IV-V.

The effect of uncertainties on the flutter behavior of the case study WF will be analyzed in Section 5.2 making use of the numerical LFT approach from Section 3.

#### 5.1.2. Case study 2: Clamped Wing (CW)

In the second case study the model consists of the same wing previously described (Fig. 7), but the inertial and elastic effects of the fuselage are not captured now.

The nominal flutter analysis is shown in Fig. 9. It is seen on the right plot that the only mode going unstable is mode I. Therefore, flutter is now triggered by an adverse coupling of the first two modes (coalescence of the frequencies of modes I-II is visible in the left plot). Moreover, instability occurs at a different speed, i.e. approximately  $V_f = 297 \frac{m}{s}$ .

The results in Figures 8-9 show that as a result of simplifications in the description of the system (for example in this case neglecting the fuselage) flutter might be wrongly estimated. In addition, different physical mechanisms might be predicted as responsible for the loss of stability. The effect of uncertainties on the flutter behavior of the case study CW will be analyzed in Section 5.3 making use of the novel symbolic LFT approach from Section 4. It will be shown that the robust analyses are able to capture the instability mechanisms not observed in the nominal analyses (Fig. 9), and only disclosed when the fuselage was considered (Fig. 8). This important result is made possible by the capability of the method to preserve the physical meaning of the uncertainties in the LFT models used for robust analysis.

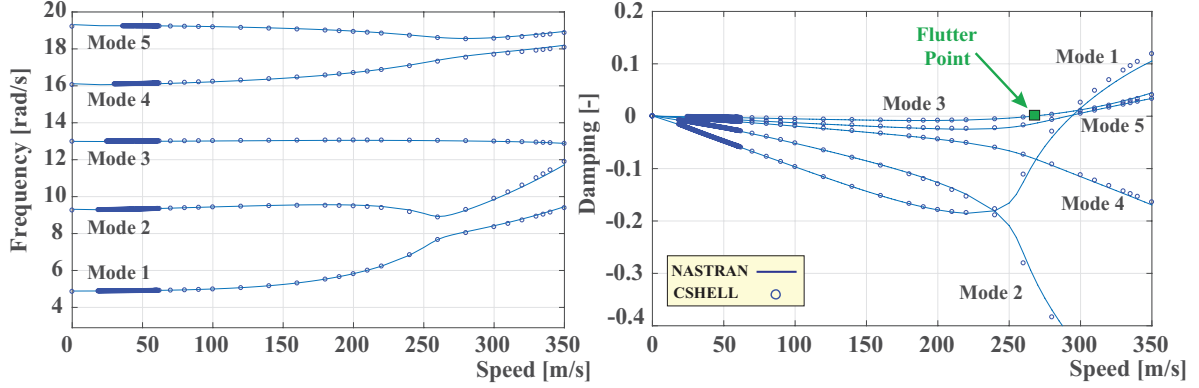


Figure 8: WF model: frequency and damping at different speeds.

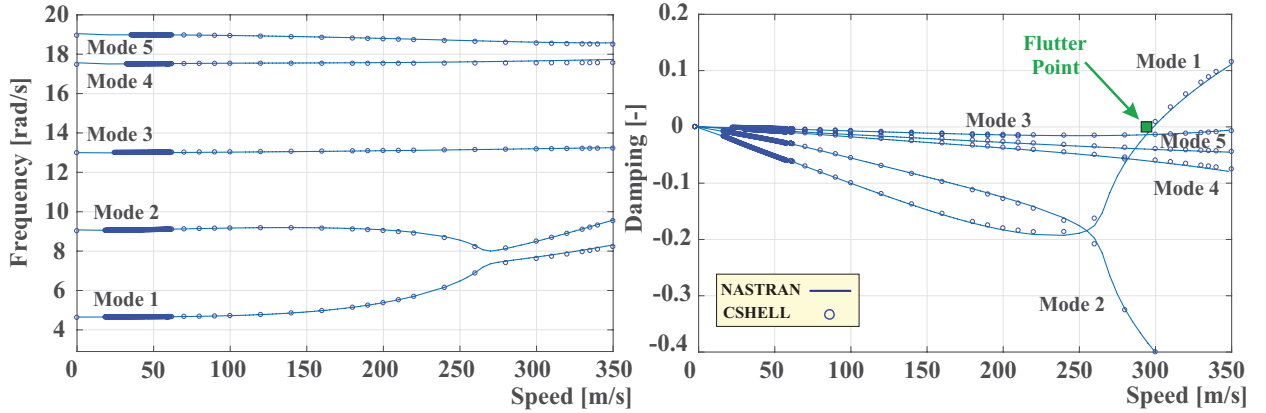


Figure 9: CW model: frequency and damping at different speeds.

### 5.2. Application of the numerical LFT approach to WF case study

The wing with elastic fuselage (WF test case) is considered here to exemplify the favourable features of the improved numerical LFT methodology proposed in Section 3.2. The first 25 structural modes ( $n_s = 25$ ) are retained in order to correctly capture flutter and this, together with the adoption of 6 lag states for the aerodynamic approximation, leads to an aeroelastic system size of 200 states.

Robust analyses are performed taking into account structural parametric uncertainties in all the concentrated fuel masses on the wing and fuselage (a total of 84 mass points). Five areas are considered: fuselage ( $f$ ); front wing root ( $w1$ ); front wing tip ( $w2$ ); rear wing tip ( $w3$ ); and rear wing root ( $w4$ ). Each of these areas has associated a value of mass  $\{Mc_f, Mc_{w1}, Mc_{w2}, Mc_{w3}, Mc_{w4}\}$  given by the sum of all the fuel masses

in that area. For each of these area masses, an independent uncertainty of 20% from their nominal values is considered. Thus the number of uncertain parameters used in the LFT will be 5, one per area. In order to proceed with the numerical construction of the LFT, a representative set of values inside the uncertainty set has to be sampled. This is done here including all the possible combinations of vertices and nominal values of the masses associated to the five stations ( $n_{pts} = 243$ ).

The corresponding two modal matrices  $\bar{\mathbf{M}}_{\mathbf{s}}$  and  $\bar{\mathbf{K}}_{\mathbf{s}}$  are then interpolated by means of the aforementioned orthogonal least-square algorithm assuming linear polynomials and considering uncertainties in the first 10 modes (i.e.  $n_{\delta} = 10$ ).

Based on the LFT of the two modal matrices, the aeroelastic LFT is assembled using the state-matrix defined in Eq. 11 and its size is reduced by means of the  $1-d$  order reduction technique [40]. The resulting uncertainty block, expressed in accordance with the definition given in Eq. (1), is:

$$\Delta_{\mathbf{M}}^{49,R} = \text{diag}(\delta_{Mc_f}^R I_9, \delta_{Mc_{w1}}^R I_{10}, \delta_{Mc_{w2}}^R I_{10}, \delta_{Mc_{w3}}^R I_{10}, \delta_{Mc_{w4}}^R I_{10}) \quad (19)$$

Note that the size of the LFT, i.e. 49, is relatively small considering the large effect that the selected uncertainties have on the interpolated quantities. The same problem, addressed by interpolating directly the state-matrices, would lead in this example to an LFT of size more than double.

Once an LFT is generated it is always required to check its accuracy. The standard approach is to sample a representative set of parameters inside  $\Delta_{\mathbf{M}}$ , and then build the corresponding *reference* state-matrices based on the structural operators computed by the FSI solver. A first (numerical) check aims to quantify the ability of the LFT to cover the samples employed to generate it. Therefore, the 243  $n_{pts}$  sampled LTIs are compared with the corresponding realizations of the LFT. The comparison is made using an analytical test based on the modal matching criterion proposed in [27]:

$$\epsilon_{modal} = \max_{i \in [1, n_{pts}]} \left( \frac{\sum_{k=1}^{n_m} |\lambda_k^i - \lambda_k^{ref,i}|}{\sum_{k=1}^{n_m} |\lambda_k^{ref,i}|} \right) \quad (20)$$

where  $\lambda_k^i$  is the LFT's  $k^{th}$  eigenvalue at sample  $i$  and  $\lambda_k^{ref,i}$  is the corresponding eigenvalue from the reference model. This test is performed at  $V_{\infty} = 260 \frac{m}{s}$  for the first six structural modes ( $n_m = 6$ ) and the result is  $\epsilon_{modal} \cong 4.8 \times 10^{-3}$ .

A second (visual) check is done by plotting the poles map of the state-matrix and comparing the reference eigenvalues (corresponding to the  $n_{pts}$  samples) and those obtained randomly sampling the parameters in  $\Delta_{\mathbf{M}}$ . This is shown in Fig. 10, where it can be appreciated that the latter (given by red crosses) lie inside the cloud of points determined by the vertices (given by blue circles). This is expected since the blue circles correspond to extreme perturbations, whereas the LFT samples are taken randomly covering all the uncertainty space. Overall, smoothness and regularity can also be appreciated in the map.

It is important to observe that, while the tests on the accuracy of the LFT models performed here are satisfactory from the point of view of capturing the effect of uncertainties on pole locations (which is of main concern in flutter analysis), other measures could be more apt to ensure other effects are captured. For example, in the case of LFT models used for control design, investigations on the time response and frequency-domain features should be also carried out [23]. In view of the discussion in Section 3.3 on the issues associated with numerically generated LFT, this is deemed an important step before using the LFT for synthesis.

After having checked the accuracy of the obtained LFT, the  $\mu$  analysis technique can be applied. Fig. 11 shows the  $\mu$  upper (UB) and lower (LB) bounds at  $V_{\infty} = 260 \frac{m}{s}$  (the nominal flutter speed is approximately  $V_f = 270 \frac{m}{s}$ ) for different values of  $n_{\delta}$ .

Consider first the case for  $n_{\delta} = 10$  (this is the LFT corresponding to Eq. (19)), and recall that the nominal analyses in Fig. 8 pointed out the occurrence of instability in nominal conditions due to mode III, but also highlighted the crossing of the zero damping line (at higher speeds) for modes I and V. It can be noted that these 3 cases also feature in the  $\mu$  plot (for the first and last peaks the numbers of the coalesced modes have been reported in the plot -recall the comments given when presenting Fig. 8), which is thus able to capture the presence of multiple elastic modes prone to cross the imaginary axis. In particular,

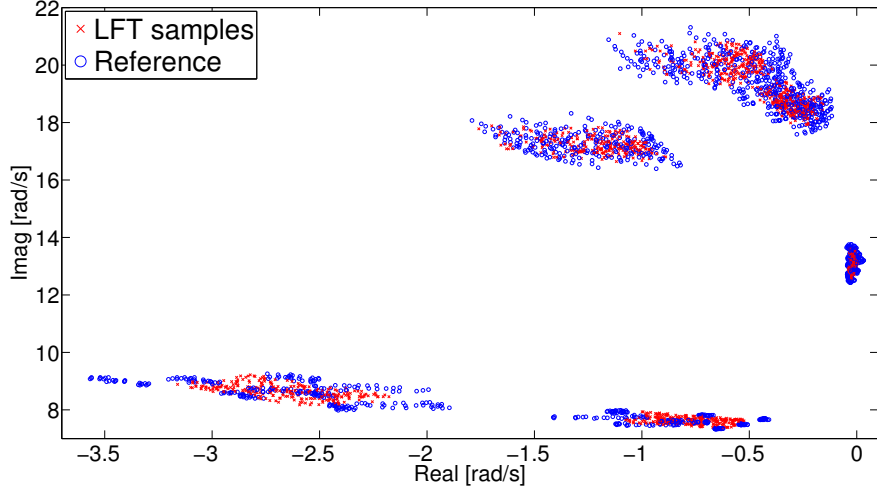


Figure 10: Poles map of the first 6 aeroelastic modes of the WF case study from sampled LFT and FSI reference solver.

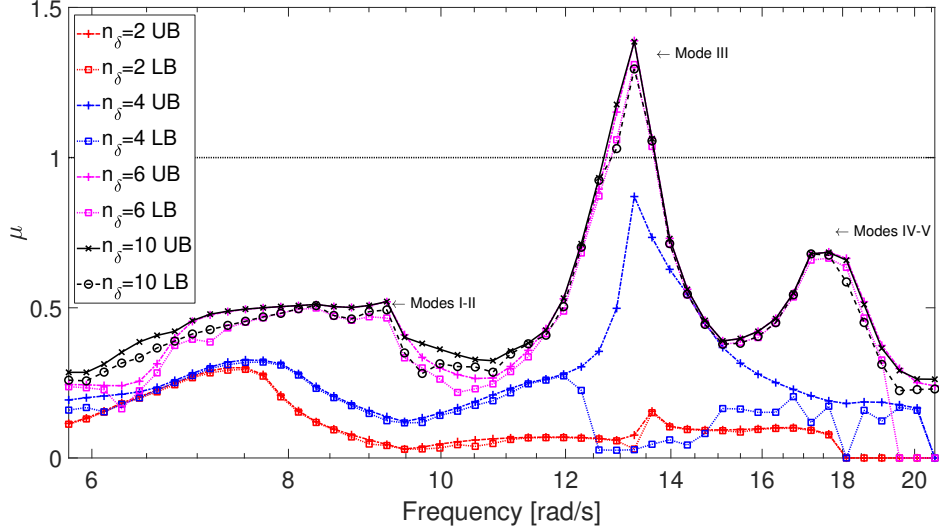


Figure 11:  $\mu$  bounds at  $V_\infty = 260 \frac{\text{m}}{\text{s}}$  for LFTs with mass uncertainties in the first  $n_\delta$  modes.

the third mode is confirmed as the most critical also in uncertain conditions (look at the first peak above  $\mu=1$  in Fig. 11, which corresponds approximately to the  $13 \frac{\text{rad}}{\text{s}}$  of the mode III flutter frequency in Fig. 8). Specifically, the system is predicted to undergo flutter at this speed with uncertainties in the allowed range ( $\mu \cong 1.35$ ). The plot corresponding to  $n_\delta = 6$  (i.e. uncertainties in the first 6 modes only) is very similar to the previous. This suggests that for robust flutter analysis purposes this reduced size LFT can be used because it captures the same effects of the uncertain parameters on the instabilities but will result in a lower LFT size to that of Eq. (19). When  $n_\delta$  is further decreased, it can be observed that not all the modes' peaks are found by the analyses and moreover the values of  $\mu$  are underestimated. For comparison with the LFT of Eq. (19) and subsequent worst-case reference, the  $\Delta$  matrix for the  $n_\delta = 6$  case is given next (note that the size has considerably reduced from 49 to 29):

$$\Delta_{\mathbf{M}}^{29,R} = \text{diag}(\delta_{M_{c_f}}^R I_5, \delta_{M_{c_{w1}}}^R I_6, \delta_{M_{c_{w2}}}^R I_6, \delta_{M_{c_{w3}}}^R I_6, \delta_{M_{c_{w4}}}^R I_6) \quad (21)$$

It is remarked here that, as discussed in Section 3.2, the possibility of performing analyses for different  $n_\delta$ ,

as those shown in Fig. 11, is enabled by the modal-oriented modelling approach used here. The benefits of such analysis range from LFT order reduction (note that the number of repetitions of the uncertain parameters is decreased from Eq. 19 to Eq. 21) to gaining insights on the role played by the uncertainties in the instabilities and so further understanding the mechanisms prompting the different instabilities. Indeed, since it is well known in aeroelasticity that instability typically arises as a result of the interaction among a restricted set of elastic modes, by isolating the effect of the perturbations on each mode this type of analysis can provide additional information.

For example, while it was expected that the LFT built with  $n_\delta = 4$  will not show the peak corresponding to the modes IV-V instability (because these modes are unperturbed in this analysis), it is interesting to see that the peak corresponding to the third mode is also not well captured. Indeed, this mode of instability is identified but the peak value is far from the one obtained with  $n_\delta = 10$ . This seems to point out that the third mode involves also higher frequency modes and thus is something more complex than the standard binary flutter concerning coalescence of only two modes.

The plot in Fig. 11 showcases also a narrow gap between upper and lower bounds for the  $n_\delta = 6$  and  $n_\delta = 10$  LFTs. This thus provides confidence on the insight obtained from inspecting the corresponding worst-case matrices. The inspection reveals (see Eq. (22) and recall the structure from Eq. (19) or Eq. (21)), that negative variations of the mass in the fuselage and front wing areas ( $f$ ,  $w1$ , and  $w2$ ) and positive variations in the rear wing areas ( $w3$  and  $w4$ ) are detrimental for the third mode flutter:

$$\begin{aligned}\Delta \mathbf{M}_{n_\delta=10}^{cr} &= \text{diag}(-0.77I_9, -0.77I_{10}, -0.77I_{10}, +0.36I_{10}, +0.59I_{10}) \\ \Delta \mathbf{M}_{n_\delta=6}^{cr} &= \text{diag}(-0.76I_5, -0.74I_6, -0.68I_6, +0.64I_6, +0.76I_6)\end{aligned}\tag{22}$$

Note that the two perturbations are qualitatively similar (they both point towards the same direction for the parameters' variation).

In order to validate the accuracy of the analyses, the concentrated masses on the fuselage and wing are modified according to Eq. (22) and a traditional (i.e. fixed parameters) flutter analysis of the perturbed systems is performed with the FSI solver. The resulting flutter speeds are in both cases approximately  $264 \frac{\text{m}}{\text{s}}$ , which is slightly larger than the value used for  $\mu$  analysis ( $V_\infty=260 \frac{\text{m}}{\text{s}}$ ). This small difference could be ascribed to the approximations made in building the LFT, as commented above. It is however important to stress that the strength of  $\mu$  consists also in identifying worst-case directions within the uncertainty set. In order to confirm this feature, extensive flutter analyses were performed in the high-fidelity FSI solver by considering perturbation matrices having magnitude equal or smaller to those in Eq. (22). All of them led to higher values of the flutter speed, confirming in this way that the two  $\Delta \mathbf{M}^{cr}$  in Eq. (22) are indeed the most critical among the tested ones.

### 5.3. Application of the symbolic LFT algorithms to CW case study

This section presents the application of the co-modeling framework presented in Section 4 to the clamped wing model (CW) introduced in Section 5.1.2.

#### 5.3.1. Robust flutter analysis of the CW case study

Uncertainties for the stiffness and mass distribution along the CW model are considered as given in Fig. 12. The FE model (depicted in Fig. 7) has 54 beam elements, enumerated as follows: the front wing is spanned by elements 1-23 (element 1-3 are part of the wing inside the fuselage), the vertical joint by elements 24-29, the aft wing by elements 30-48 and the fin by elements 49-54. From these beam elements, 27 stations (shown and numbered in Fig. 12(a)) are defined by pairing consecutive beams and for each of them the bending stiffness parameter  $EI_z$  is considered uncertain. As a result, the stiffness uncertainty description consists of 27 uncertainties (i.e.  $\delta_{EI_{z_j}}$  with  $j=1,\dots,27$ ) which are allowed to vary independently within 10% of their nominal values. As for the mass, the model has 36 fuel masses  $m_f$  distributed between the front and rear wings (shown and numbered in Fig. 12(b)). These are all assumed parametric uncertainties (i.e.  $\delta_{m_{f_k}}$  with  $k=1,\dots,36$ ) which are allowed to vary independently within 10% of their nominal values. Thus, there are in total 63 parametric uncertainties.

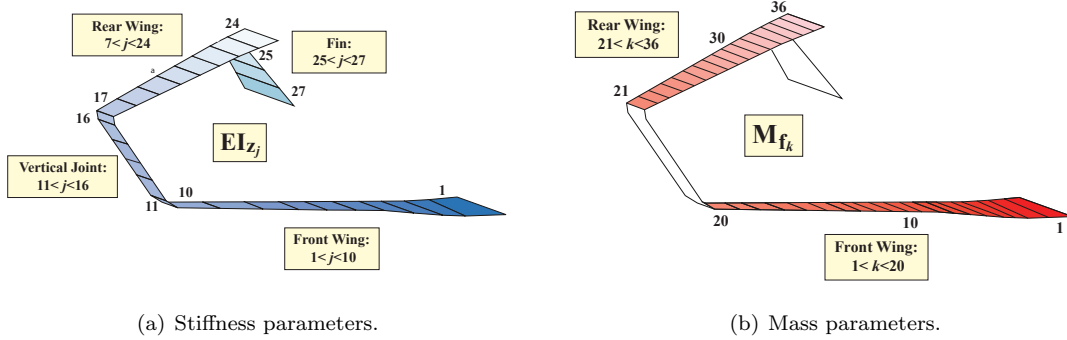


Figure 12: Uncertainty description for the Clamped Wing (CW) test case.

With the above uncertainty definitions, it is possible to apply the symbolic LFT modeling strategy described in Algorithm 1. Despite the adoption of order reduction techniques [40], the LFT has an uncertainty block of size  $\Delta_{\mathbf{M}-\mathbf{K}}^{630,R}$ . While its accuracy in capturing the variability of the structural matrices was confirmed by tests similar to the one depicted in Fig. 10, its size is such that it cannot be used for  $\mu$  analysis. The large number of uncertain parameters was initially considered in order to showcase the modeling possibilities (especially when compared to the numerical approach), but in a second step a reduced-order LFT of dimension 225,  $\Delta_{\mathbf{M}-\mathbf{K}}_{red}^{225,R}$ , is obtained by leveraging distinctive features of this approach, namely the modal-oriented aspect and the availability of a symbolic expression for the dependence of the structural matrices on the uncertainties. Further details on this order reduction can be found in [15] and are omitted here for brevity.

Algorithm 2 can then be applied. The analysis detects a worst-case perturbation that makes the aeroelastic system flutter at the selected subcritical speed  $V_\mu$ . For the present case,  $V_\mu = 285 \frac{\text{m}}{\text{s}}$  is chosen considering the flutter behaviour of the nominal configuration ( $V_f = 297 \frac{\text{m}}{\text{s}}$  from Fig. 9). Fig. 13 shows the upper bounds of  $\mu$  obtained in the first four iterations (ITER#) of Algorithm 2. The lower bound at ITER 1 was shown in [15] and is close to the corresponding upper bound curve in the range of frequencies relative to the highest peak.

Note that two peaks are clearly observed, a lower frequency one, taking place at approximately  $\omega_1 = 7.2 \frac{\text{rad}}{\text{s}}$  and associated with the coalesced modes I-II, and a higher frequency one (at  $\omega_2 = 13.2 \frac{\text{rad}}{\text{s}}$ ) representing the mode III flutter. This highlights an important feature of the proposed robust modeling analysis framework (and of the application of  $\mu$  analysis for the robust flutter problem in general [5]). Indeed, nominal analyses (Fig. 9) detected that modes I-II were the only responsible for flutter (note that mode III is stable over the whole range of speeds). It was necessary to augment the CW model with an elastic fuselage (i.e. the CWF model) for the nominal analyses to find that mode III is also critical for the instability. As seen in Fig. 13, robust analyses for the uncertain CW model feature both of these unstable mechanisms when variations of stiffness and mass parameters are allowed. In other words, a more simplified description of the same system (model *CW*) is able to provide the same information gathered by a more refined one (model *WF*) when the model is augmented with uncertainties having a precise physical meaning. This result should be interpreted by recalling that the uncertainties in Fig. 12 have a clear physical meaning (e.g. perturbation in the wing's skin thickness), and thus only certain *modes* are introduced in the perturbed system which have the potential to make it unstable. This is a different scenario than that arising when fictitious uncertainties, e.g. in the natural frequencies or damping ratios, are considered. In view of this, the fact that Fig. 13 captures the mode III instability is deemed an important result and a confirmation of the accuracy offered by the developed framework.

As prescribed by the analysis algorithm, the worst-case matrix extracted from the highest peak of the lower bound is used, and hence the instability related to the coalescence of modes I-II (featuring a peak value

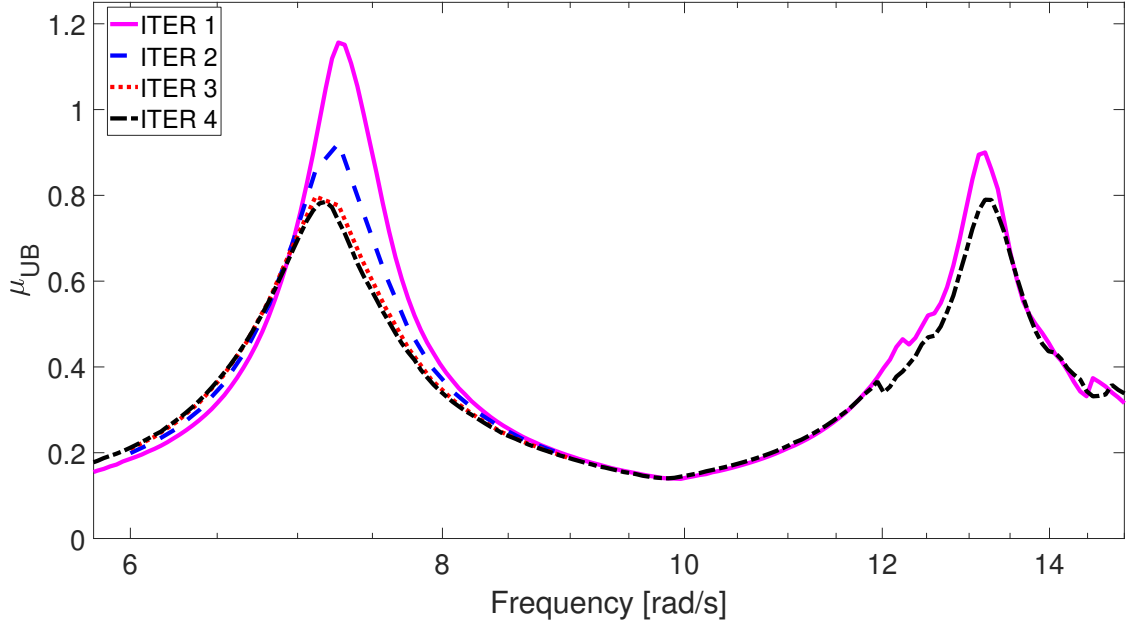


Figure 13:  $\mu_{UB}$  obtained with the symbolic algorithm at  $V_\infty = 285 \frac{m}{s}$ . Convergence is attained at the 4<sup>th</sup> iteration.

of  $\mu \cong 1.15$  at  $\omega \cong 8 \frac{rad}{s}$ ) is studied here. Tab. 1 reports, at each iteration, the flutter speed  $V_{f\mu}$  (calculated by CSHELL) as well as the perturbations for each uncertain parameter. For the benefit of readability, the columns are labelled with the symbol of the parameter (e.g.  $EI_{z_1}$ ), but the reported values have to be interpreted as normalized perturbations (e.g.  $\delta EI_{z_1}$ ). The last column also shows the norm of the critical perturbation matrix.

The algorithm achieves in 4 iterations a value of  $V_{f\mu} = 285.2 \frac{m}{s}$  which is within 0.15% of the selected  $V_\mu = 285 \frac{m}{s}$ . At each iteration #, the magnitude of  $\Delta_{ITER\#}^{cr}$  increases (this was already noticeable from Fig. 13 since smaller  $\mu_{UB}$  indicates larger absolute values for the worst-case). The change in magnitude of  $\Delta_{ITER\#}^{cr}$  can be related to the importance of the perturbations in the modal base  $\Phi$ , not captured in the standard LFT representation but taken into account with the iterative strategy (recall the interpretation given in Eq. 18). Crucially, since  $\bar{\sigma}(\hat{\Delta}^{cr}) = \bar{\sigma}(\Delta_{ITER4}^{cr}) = 1.47 > 1$ , it can be concluded that the joined-wing is guaranteed to be robustly stable at  $V_\infty = 285 \frac{m}{s}$  in the face of the allowed modeling uncertainties.

### 5.3.2. Optimality analysis of the worst-case perturbation

A careful evaluation of Table 1 reveals that the perturbations show approximately the same directionality from one iteration to the other (e.g. positive/negative trends of the uncertain parameters). This qualitatively supports the accuracy of the predicted  $\hat{\Delta}^{cr}$ , and more generally indicates that worst-case regions are correctly detected (further comments on this are given in the next section). This pattern is favourable since robustness properties such as flutter sensitivity to a set of selected physical parameters [5] can be approximately captured without updating the modal matrix (i.e. using the nominal  $\Phi_0$ ).

However, two uncertain parameters requiring subsequent detailed analysis are identified, namely  $EI_{z_5}$  and  $m_{f_{21}}$ , which exhibited a non-uniform pattern. The former has an almost null perturbation in  $\Delta_{ITER1}^{cr}$  but then becomes positive for the other iterations, whereas  $m_{f_{21}}$  changes sign at the second iteration. By performing a  $\mu$  sensitivity analysis, it can be concluded that the parameter  $EI_{z_5}$  has small importance for flutter, whereas  $m_{f_{21}}$  (a rear wing tip mass) is proved to be relevant for the instability.

The optimality check proposed in Algorithm 3 is applied to investigate the behavior of  $m_{f_{21}}$ , and in order to do so the tested perturbation matrices  $\Delta_i^t$  must be selected (Step-C1 of the algorithm). Table 2 reports the definition for the 5 tested LFTs, along with the resulting  $\mu_{UB}$ . The LFTs are centered at: the perturbation matrix  $\Delta_{ITER1}^{cr}$  found in the first iteration (i.e. first row in Table 1), this LFT is termed

Table 1: Perturbation matrix  $\Delta_{\text{ITER}\#}^{cr}$  and corresponding speed  $V_{f\mu}$  at each iteration.

ITER	$V_{f\mu} \left[ \frac{\text{m}}{\text{s}} \right]$	$EI_{z_1}$	$EI_{z_2}$	$EI_{z_3}$	$EI_{z_4}$	$EI_{z_5}$	$EI_{z_6}$	$EI_{z_7}$	$EI_{z_8}$	$EI_{z_9}$	$EI_{z_{10}}$
1	288.4	-0.98	-0.98	-0.98	-0.98	0.082	0.98	0.98	-0.98	-0.98	-0.98
2	287.4	-1.23	-1.23	-1.23	-1.23	1.08	1.23	1.23	-1.23	-1.23	-1.23
3	285.9	-1.41	-1.41	-1.41	-1.41	1.37	1.41	1.41	-1.41	-1.41	-1.41
4	285.24	-1.47	-1.47	-1.47	-1.47	1.47	1.47	1.47	-1.47	-1.47	-1.47
$EI_{z_{13}}$	$EI_{z_{15}}$	$EI_{z_{17}}$	$EI_{z_{18}}$	$EI_{z_{19}}$	$EI_{z_{20}}$	$EI_{z_{21}}$	$EI_{z_{22}}$	$EI_{z_{23}}$	$EI_{z_{24}}$	$m_{f_7}$	$m_{f_8}$
-0.98	0.98	-0.98	-0.98	0.98	0.98	-0.98	-0.98	-0.98	-0.98	0.98	0.98
-1.23	1.23	-1.23	-1.23	1.23	1.23	-1.23	-1.23	-1.23	-1.23	1.23	1.23
-1.41	1.41	-1.41	-1.41	1.41	1.41	-1.41	-1.41	-1.41	-1.41	1.41	1.41
-1.47	1.47	-1.47	-1.47	1.47	1.47	-1.47	-1.47	-1.47	-1.47	1.47	1.47
$m_{f_9}$	$m_{f_{10}}$	$m_{f_{11}}$	$m_{f_{12}}$	$m_{f_{13}}$	$m_{f_{14}}$	$m_{f_{15}}$	$m_{f_{16}}$	$m_{f_{17}}$	$m_{f_{18}}$	$m_{f_{19}}$	$m_{f_{20}}$
0.98	0.98	0.98	0.98	0.98	0.98	0.98	0.98	0.98	0.98	-0.98	-0.98
1.23	1.23	1.23	1.23	1.23	1.23	1.23	1.23	1.23	1.23	-1.23	-1.23
1.41	1.41	1.41	1.41	1.41	1.41	1.41	1.41	1.41	1.41	-1.41	-1.41
1.47	1.47	1.47	1.47	1.47	1.47	1.47	1.47	1.47	1.47	-1.47	-1.47
$m_{f_{21}}$	$m_{f_{22}}$	$m_{f_{23}}$	$m_{f_{24}}$	$m_{f_{25}}$	$m_{f_{26}}$	$m_{f_{27}}$	$m_{f_{28}}$	$m_{f_{29}}$	$m_{f_{30}}$	$m_{f_{31}}$	$\bar{\sigma}(\Delta^{cr})$
0.82	0.98	0.92	0.98	0.98	0.98	0.98	0.98	0.98	0.98	0.98	0.98
-1.23	1.18	1.23	1.23	1.23	1.23	1.23	1.23	1.23	1.23	1.23	1.23
-1.3	1.39	1.41	1.41	1.41	1.41	1.41	1.41	1.41	1.41	1.41	1.41
-1.09	1.47	1.47	1.47	1.47	1.47	1.47	1.47	1.47	1.47	1.47	1.47

1-1; the opposite of  $\Delta_{\text{ITER}1}^{cr}$  (case 1-2); the second iteration critical perturbation  $\Delta_{\text{ITER}2}^{cr}$  (case 2-1); the opposite of  $\Delta_{\text{ITER}2}^{cr}$  (case 2-2); and a special case of  $\Delta_{\text{ITER}2}^{cr}$  which considers an opposite perturbation in the tip mass  $m_{f_{21}}$  (i.e. positive instead of the negative predicted at this iteration) (case 2-3).

Table 2: Tested worst-case perturbations in the optimality check.

case	ITER	$\Delta_i^t$	$\mu_{\text{UB}}$
1-1	1	$\Delta_{\text{ITER}1}^{cr}$	4.4
1-2	1	$-\Delta_{\text{ITER}1}^{cr}$	0.53
2-1	2	$\Delta_{\text{ITER}2}^{cr}$	6.3
2-2	2	$-\Delta_{\text{ITER}2}^{cr}$	0.44
2-3	2	$\Delta_{\text{ITER}2}^{cr}, \delta_{m_{f,21}} = -\delta_{m_{f,21}}^{cr}$	9

Fig. 14 shows the results which, for a better visualisation, feature reversed axes with respect to the usual convention, i.e.  $\mu_{\text{UB}}$  plotted on the  $x$ -axis and  $\omega$  on the  $y$ -axis. For comparison purposes, the curves from Fig. 13 for iteration 1 (ITER 1) and iteration 2 (ITER 2) are presented as solid lines with cross and square markers respectively.

Consider first the curves relative to the first iteration, that is 1-1 (blue dash-dot line) and 1-2 (blue dotted line). The dash-dot line has a higher peak than the one featured by ITER 1, whereas the dotted



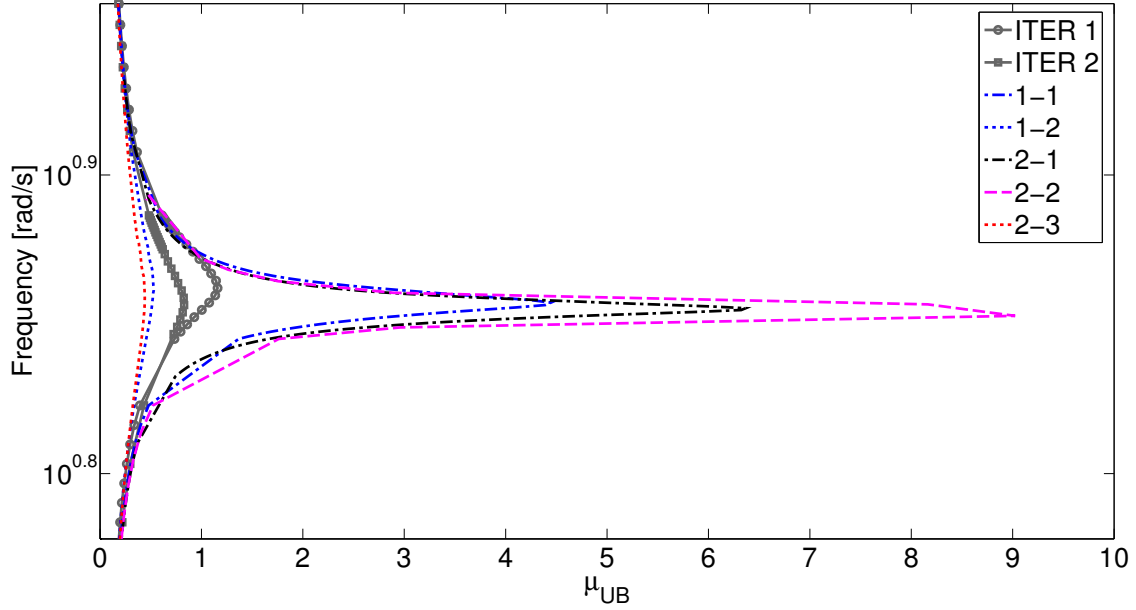


Figure 14:  $\mu$  analysis of LFTs featuring different nominal plants. The value of the peak is a measure of the proximity of the nominal plant to the actual worst-case.

line has the smallest (among these 3). This, along with the noticeable sharp peak of the dash-dot curve, suggests that  $\Delta_{\text{ITER1}}^{cr}$  points at a worst-case direction for the system. It is stressed that Algorithm 3 builds each LFT based on the modal base  $\Phi$  associated with the tested worst-case perturbation (Step-C3). Note that when an LFT associated with an actual worst-case perturbation matrix predicted by  $\mu$  is tested (e.g. case 1-1), in principle the nominal plant has a pole on the imaginary axis and thus one would expect the  $\mu$  peak to be infinitely large (recall its definition in Eq. 5). However, the worst-case perturbation matrix is obtained with an LFT built up with a different modal matrix  $\Phi$ . Therefore, the nominal plant does not have a purely complex pole and the procedure is numerically reliable, as it will be apparent next.

The analyses performed with respect to the results from the second iteration are considered next -these correspond to cases 2-1 (black dash-dot line), 2-2 (red dotted line), and 2-3 (magenta dashed line). A first remark is that the  $\mu$  upper bound for 2-1 exceeds 1-1, meaning that as the algorithm proceeds, it converges to the worst-case of the system (i.e.  $\Delta_{\text{ITER2}}^{cr}$  is a better estimation of  $\Delta^{cr}$  than  $\Delta_{\text{ITER1}}^{cr}$ ). Another important aspect is inferred by comparing the magenta (2-3) and black (2-1) curves. The former has a greater peak than the latter, that is, the  $\mu_{\text{UB}}$  algorithm detects case 2-3 as a closer worst-case of the system than 2-1. In other words, the worst perturbation for  $m_{f_{21}}$  is the positive one (as initially predicted in the first iteration). Interestingly, the peak of  $\mu$  is not infinitely large for 2-1 (in fact, there exists another LFT with larger peak), which shows that the algorithm is numerically well-posed and is able to capture the effect of updating the modal base on the global optimum. Similar evidences on the role of parameter  $m_{f_{21}}$  are obtained by applying these analyses for ITER 3.

Prompted by these findings, the iterative cycle is restarted at ITER 2 with the perturbation matrix  $\Delta_{\text{ITER2}}^{cr}$  but enforcing a positive perturbation in  $m_{f_{21}}$ . Inspired by hybrid strategies common in applied optimisation [36], the idea is to initialise the (non-convex) algorithm with the best candidate in the population (represented by the three tested  $\Delta_i^t$ ) according to the cost function, which is here the peak of  $\mu$  in the plots of Fig. 14. The new iterative cycle only requires 3 iterations to converge, and the perturbation matrix at the last iteration has a norm  $\bar{\sigma}(\Delta_{\text{ITER3-new}}^{cr}) \cong 1.34$ , whereas before (see Table 1) it was  $\bar{\sigma}(\Delta_{\text{ITER4}}^{cr}) \cong 1.47$ . Thus, the perturbation identified thanks to Algorithm 3 has indeed a smaller norm. These analyses confirm that the proposed heuristic approach to check the correctness of the worst-case matrix can provide a helpful tool to monitor the accuracy of the results.

## 6. Conclusions

The paper deals with methodologies to address the development of uncertainty descriptions for aeroelastic systems by merging the robust modeling paradigm LFT with representative fluid-structure interaction solvers. It also proposes strategies to perform reliable and profitable analyses of such uncertain models within the LFT- $\mu$  robust control paradigm. In order to showcase the applicability of the methods, an unconventional joined-wing configuration called PrandtlPlane is considered as test case.

Two LFT-FSI modeling approaches are presented. The symbolic LFT approach allows the uncertainty modeling to be performed in parallel with the assembly of the structural operators in the FSI solvers. The advantages of this approach range from an enhanced flexibility in the parameters' selection (very localized uncertainties can be captured) to a direct connection between uncertainties in the LFT model and physical quantities in the high-order model. The approximations involved by this approach are critically discussed, and an iterative algorithm, which updates the structural modes based on the worst-case predicted by  $\mu$ , is proposed. Its application leads to predictions validated in the FSI solver, and shows good agreement with previous findings from the literature.

The work also shows the application of a numerical LFT approach for constructing LFTs of high-order systems in a more efficient way. Advantages in terms of LFT size's reduction, easier identification of the different modes for scattered values of the uncertain parameters, and the possibility of performing multiple analyses which might enhance understanding of the investigated phenomenon are commented with reference to the studied examples.

The work showcases the potential of the LFT- $\mu$  framework in addressing the challenging flutter problem of complex aircraft configurations subject to a large set of uncertainties, of which Joined Wings are a paradigmatic example.

## Acknowledgements

This work was partially funded by the European Union's Horizon 2020 research and innovation programme under grant agreement No 636307, project FLEXOP, and was performed during the first author's doctoral studies at the University of Bristol. The authors wish to thank the ONERA SMAC team for providing the version of the APRICOT's routine *olsapprox* in the early stages of this work (at present the full version of the APRICOT library is freely available to download from the SMAC website).

## References

- [1] W. P. Rodden, Theoretical and Computational Aeroelasticity, Crest Publishing, 2011.
- [2] K. Zhou, J. C. Doyle, K. Glover, Robust and Optimal Control, Prentice-Hall, Inc., 1996.
- [3] Lind, R. and Brenner, M., Robust Aeroservoelastic Stability Analysis, Advances in Industrial Control, Springer, 2012.
- [4] D. Borglund, The  $\mu$ -k Method for Robust Flutter Solutions, Journal of Aircraft 41 (5) (2004) 1209–1216.
- [5] A. Iannelli, A. Marcos, M. Lowenberg, Study of Flexible Aircraft Body Freedom Flutter with Robustness Tools, Journal of Guidance, Control, and Dynamics 41 (5) (2018) 1083–1094.
- [6] A. Iannelli, A. Marcos, M. Lowenberg, Aeroelastic modeling and stability analysis: A robust approach to the flutter problem, International Journal of Robust and Nonlinear Control 28 (1) (2018) 342–364.
- [7] C. Poussot-Vassal, C. Roos, Generation of a reduced-order LPV/LFT model from a set of large-scale MIMO LTI flexible aircraft models, Control Engineering Practice 20 (9) (2012) 919–930.
- [8] S. Bennani, B. Beuker, J. van Staveren, J. Meijer, Flutter Analysis for the F-16A/B in Heavy Store Configuration, Journal of Aircraft 42 (6) (2005) 1566–1575.
- [9] P. Apkarian, M. N. Dao, D. Noll, Parametric robust structured control design, IEEE Transactions on Automatic Control 60 (7) (2015) 1857–1869.
- [10] D. Navarro-Tapia, A. Marcos, S. Bennani, C. Roux, Structured H-infinity Control Design for the VEGA Launcher: Robust Control Design Augmentation, in: International Astronautical Congress (IAC), 2018.
- [11] J. Veenman, C. W. Scherer, H. Koroğlu, Robust stability and performance analysis based on integral quadratic constraints, European Journal of Control 31 (2016) 1–32.
- [12] A. Iannelli, A. Marcos, M. Lowenberg, Nonlinear robust approaches to study stability and postcritical behavior of an aeroelastic plant, IEEE Transactions on Control Systems Technology 27 (2) (2019) 703–716.
- [13] D. Dal Canto, A. Frediani, G. L. Ghiringhelli, M. Terraneo, The lifting system of a PrandtlPlane, part 1: Design and analysis of a light alloy structural solution, in: G. Buttazzo, A. Frediani (Eds.), Variational Analysis and Aerospace Engineering: Mathematical Challenges for Aerospace Design, 2012, pp. 211–234.

- [14] R. Cavallaro, L. Demasi, Challenges, ideas, and innovations of joined-wing configurations: A concept from the past, an opportunity for the future, *Progress in Aerospace Sciences* 87 (2016) 1 – 93.
- [15] A. Iannelli, A. Marcos, R. Bombardieri, R. Cavallaro, A symbolic LFT approach for robust flutter analysis of high-order models, *IEEE European Control Conference*, 2019.
- [16] J. Doyle, Analysis of feedback systems with structured uncertainties, *IEEE Proceedings D Control Theory and Applications* 129 (6) (1982) 242–250.
- [17] L. Demasi, E. Livne, Dynamic Aeroelasticity of Structurally Nonlinear Configurations Using Linear Modally Reduced Aerodynamic Generalized Forces, *AIAA Journal* 47 (2009) 71–90.
- [18] R. Cavallaro, R. Bombardieri, L. Demasi, A. Iannelli, Prandtlplane Joined Wing: Body freedom flutter, limit cycle oscillation and freeplay studies, *Journal of Fluids and Structures* 59 (2015) 57–84.
- [19] T. Belytschko, W. Liu, B. Moran, *Nonlinear finite elements for continua and structures*, Wiley, 2000.
- [20] K. Roger, *Airplane math modeling methods for active control design*, AGARD-CP-228.
- [21] J. Dettman, *Mathematical Methods in Physics and Engineering*, Dover Books on Engineering, Dover, 1969.
- [22] A. Marcos, G. Balas, Development of Linear Parameter Varying Models for Aircraft, *Journal of Guidance, Control, and Dynamics* 27 (2) (2004) 218–228.
- [23] A. Iannelli, P. Simplicio, D. Navarro-Tapia, A. Marcos, LFT Modeling and  $\mu$  Analysis of the Aircraft Landing Benchmark, in: *20th IFAC World Congress*, 2017.
- [24] J. Magni, Linear fractional representation toolbox modelling, order reduction, gain scheduling, Technical Report TR 6/08162, DCSD, ONERA, Systems Control and Flight Dynamics Department (2004).
- [25] S. Hecker, A. Varga, Generalized LFT-Based Representation of Parametric Uncertain Models, *European Journal of Control* 10 (4) (2004) 326 – 337.
- [26] A. Marcos, D. Bates, I. Postlethwaite, A symbolic matrix decomposition algorithm for reduced order linear fractional transformation modelling, *Automatica* 43 (7) (2007) 1211 – 1218.
- [27] J. Torralba, F. Demourant, G. Puyou, G. Ferreres, A Method for Flexible Aircraft LFT Modelling, *IEEE European Control Conference*, 2009.
- [28] C. Roos, G. Hardier, J.-M. Biannic, Polynomial and rational approximation with the APRICOT library of the SMAC toolbox, *Proceedings of the IEEE Multiconference on Systems and Control*, 2014.
- [29] MathWorks, *Symbolic Math Toolbox version 8.0.0*, Natick, Massachusetts, 2017.
- [30] S. Hecker, A. Varga, J.-F. Magni, Enhanced lfr-toolbox for matlab, *Aerospace Science and Technology* 9 (2) (2005) 173 – 180.
- [31] B. Moulin, M. Idan, M. Karpel, Aeroservoelastic Structural and Control Optimization Using Robust Design Schemes, *J. of Guidance, Control and Dynamics* 25 (1) (2002) 152–159.
- [32] F. Chavez, D. Schmidt, Systems approach to characterizing aircraft aeroelastic model variation for robust control applications, *AIAA Guidance, Navigation, and Control Conference*, 2001.
- [33] S. Heinze, D. Borglund, Robust Flutter Analysis Considering Mode Shape Variations, *Journal of Aircraft* 45 (3) (2008) 1070–1074.
- [34] P. Seiler, A. Packard, G. J. Balas, A gain-based lower bound algorithm for real and mixed  $\mu$  problems, *Automatica* 46 (3) (2010) 493–500.
- [35] C. Roos, Systems modeling, analysis and control (SMAC) toolbox: An insight into the robustness analysis library, in: *2013 IEEE Conference on Computer Aided Control System Design (CACSD)*, 2013.
- [36] P. P. Menon, J. Kim, D. G. Bates, I. Postlethwaite, Clearance of Nonlinear Flight Control Laws Using Hybrid Evolutionary Optimization, *IEEE Transactions on Evolutionary Computation* 10 (6) (2006) 689–699.
- [37] A. Frediani, V. Cipolla, E. Rizzo, The PrandtlPlane configuration: Overview on possible applications to civil aviation, in: G. Buttazzo, A. Frediani (Eds.), *Variational Analysis and Aerospace Engineering: Mathematical Challenges for Aerospace Design*, Vol. 66 of *Springer Optimization and Its Applications*, Springer US, 2012, pp. 179–210, 10.1007/978-1-4614-2435-2.8.
- [38] F. Oliviero, Preliminary design of a very large PrandtlPlane freighter and airport network analysis, Ph.D. thesis, Università di Pisa (December 2015).
- [39] W. P. Rodden, E. H. Johnson, *User Guide V 68 MSC/NASTRAN Aeroelastic Analysis*, 1994.
- [40] P. Lambrechts, J. Terlouw, S. Bennani, M. Steinbuch, Parametric uncertainty modeling using LFTs, *Proc. of the American Control Conference*, 1993.